NAVAL POSTGRADUATE SCHOOL
Monterey, California

AD-A241 700

DTIC
ELECTE
OCT. 28 1991
S B D

THESIS

MAGNETIC FIELDS AND ELECTRON TRAJECTORIES
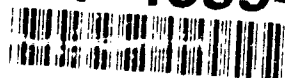AT THE END OF A HELICAL UNDULATOR

by

Daniel Ergen Craun

December 1990

Thesis Advisor: Wm. B. Colson

Approved for public release; distribution is unlimited.

91-13994

REPORT DOCUMENTATION PAGE

Form Approved
OMB No 0704-0188

1a REPORT SECURITY CLASSIFICATION Unclassified		1b RESTRICTIVE MARKINGS			
2a SECURITY CLASSIFICATION AUTHORITY		3 DISTRIBUTION/AVAILABILITY OF REPORT Approved for public release Distribution is unlimited			
2b DECLASSIFICATION/DOWNGRADING SCHEDULE					
4 PERFORMING ORGANIZATION REPORT NUMBER(S)		5 MONITORING ORGANIZATION REPORT NUMBERS)			
6a NAME OF PERFORMING ORGANIZATION Naval Postgraduate School	6b OFFICE SYMBOL (If applicable) PH	7a NAME OF MONITORING ORGANIZATION Naval Postgraduate School			
6c ADDRESS (City, State, and ZIP Code) Monterey, Calif. 93943-5000		7b ADDRESS (City State and ZIP Code) Monterey, Calif. 93943-5000			
8a NAME OF FUNDING SPONSORING ORGANIZATION	8b OFFICE SYMBOL (If applicable)	9 PROCUREMENT INSTRUMENT IDENTIFICATION NUMBER			
8c ADDRESS (City, State and ZIP Code)		10 SOURCE OF FUNDING NUMBERS			
		PROGRAM ELEMENT NO	PROJECT NO	TASK NO	WORK UNIT ACCESSION NO

11 TITLE (Include Security Classification)

MAGNETIC FIELDS AND ELECTRON TRAJECTORIES AT THE END OF A HELICAL UNDULATOR

12 PERSONAL AUTHOR(S)

Craun, Daniel E.

13a TYPE OF REPORT Masters Thesis	13b TIME COVERED FROM _____ TO _____	14 DATE OF REPORT (Year, Month Day) December 20, 1990	15 PAGE COUNT 86

16 SUPPLEMENTARY NOTATION The views expressed in this thesis were those expressed by the author and do not reflect the official policy or position of the Department of of Defense or the U.S. government.

17 COSATI CODES			18 SUBJECT TERMS (Continue on reverse if necessary and identify by block number)
FIELD	GROUP	SUB-GROUP	Simulation, current element integration, compact FEL undulator design representation, magnetic field representation, Electron trajectory representation.

19 ABSTRACT (Continue on reverse if necessary and identify by block number)

An undulator is a periodic magnetic field device that is an integral part of a Free Electron Laser (FEL). The key to FEL performance is the undulator design. This thesis models the undulator magnetic fields by using the Biot-Savart law, a current element integration technique. Applying this technique to different winding schemes for a bifilar helical compact undulator, the field structure is computed for positions outside the entrance to the undulator. These stray fields can have a focusing or defocusing effect on the incoming electron beam. This disturbs the critical matching of the electron velocity vectors with the co-propagating laser radia-

20 DISTRIBUTION/AVAILABILITY OF ABSTRACT ☒ UNCLASSIFIED UNLIMITED ☐ SAME AS RPT ☐ DTIC USERS	21 ABSTRACT SECURITY CLASSIFICATION Unclassified	
22a NAME OF RESPONSIBLE INDIVIDUAL William B. Colson	22b TELEPHONE (Include Area Code) (408) 646-2765	22c OFFICE SYMBOL PH/Cw

tion. The matching of velocity vectors controls the bunching of the electrons. This bunching action controls the gain of the FEL, and thus, the ultimate performance of the entire device. By choosing a better design for the undulator, this unwanted effect is reduced.

The field structure found from integration determines the electron trajectories. The best design for the undulator is then determined by the imposed input conditions on the electron beam for entry into the cavity. An additional benefit of this technique is a potential application to finding coil winding tolerances for undulator construction.

DD Form 1473, JUN 86 (Reverse)

MAGNETIC FIELDS AND ELECTRON TRAJECTORIES
AT THE END OF A HELICAL UNDULATOR

by

Daniel E. Craun

Lieutenant, United States Navy

B.S., United States Naval Academy,1982

Submitted in partial fulfillment of the
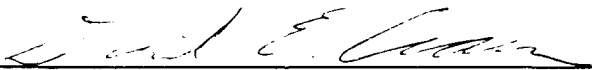
requirements for the degree of

MASTER OF SCIENCE IN PHYSICS

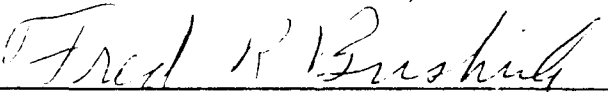from the

NAVAL POSTGRADUATE SCHOOL

December 1990

Author: _____

Daniel E Craun

Approved by: _____

William B. Colson, Thesis Advisor

_____

Fred Ramon Buskirk, Second Reader

_____

Karlheinz E. Woehler, Chairman,

Department of Physics

iii

ABSTRACT

An undulator is a periodic magnetic field device that is an integral part of a Free Electron Laser (FEL). The key to FEL performance is the undulator design. This thesis models the undulator magnetic fields by using the Biot-Savart law, a current element integration technique. Applying this technique to different winding schemes for a bifilar helical compact undulator, the field structure is computed for positions outside the entrance to the undulator. These stray fields can have a focusing or defocusing effect on the incoming electron beam. This disturbs the critical matching of the electron velocity vectors with the co-propagating laser radiation. The matching of velocity vectors controls the bunching of the electrons. This bunching action controls the gain of the FEL, and thus, the ultimate performance of the entire device. By choosing a better design for the undulator, this unwanted effect is reduced.

The field structure found from integration determines the electron trajectories. The best design for the undulator is then determined by the imposed input conditions on the electron beam for entry into the cavity. An additional benefit of this technique is a potential application to finding coil winding tolerances for undulator construction.

iv

Table of Contents

ACKNOWLEDGEMENT

This work would not have been possible without the advice, direction and support of Professor William Colson. No matter what he was doing, he always made time to discuss this work. Also, I would like to thank the Naval Postgraduate School, who managed to get the computer workstations in time to enable me to do the numerous simulations needed in a reasonable amount of time.

Most of all, I wish to express my appreciation to my wife, Laury, who put up with my neglect and absence for the longest time. Without her love and support, I would surely have failed in this endeavour.

I. INTRODUCTION

One of the designs proposed for a Directed Energy Weapon capable of delivering large amounts of energy at a considerable distance at the speed of light is the Free Electron Laser (FEL). The FEL uses a relativistic electron beam as a power source coupled to the radiation inside of an undulator. The FEL has many of the same attributes as ordinary lasers, such as coherence, high rate of fire and high energy density [1]. The FEL additionally has the ability to be tuned over a large range of wavelengths which increases its flexibility for diverse laboratory applications, and as a speed of light weapon, can be tuned for maximum atmospheric propagation.

The key to the performance of the FEL is the undulator design. The undulator bends an incoming relativistic electron beam back and forth resulting in the emission of photons in the forward direction. If the undulator is placed inside a laser resonance cavity, and the dimensions are adjusted appropriately, a FEL is made which has the capability to tune the output radiation. The undulator defines the magnetic field structure, and thus controls the electron trajectories. Therefore, the exact position and velocity of the individual electrons is dependent on the design of the undulator. The electron positions and velocities in the co-propagating laser radiation are critical to the evolution of electron bunching. This electron bunching is responsible for the high energy transfer (gain) between the electron beam and the light. This gain determines important aspects of the performance of the FEL. Since the undulator controls the gain achieved, the chosen design of the undulator will limit the ultimate performance of the FEL.

This thesis models the undulator magnetic fields using the Biot-Savart law. Using this current element integration technique, we apply it to different winding schemes for a bifilar compact undulator. The field structure can then be computed

1

for positions outside the entrance to the undulator. These stray fields can have a focusing or defocusing effect on the incoming electron beam. The matching of the electron velocity vectors with the co-propagating laser radiation is essential to the energy transfer from the electrons to the light. The energy transfer between them is called coupling. This coupling controls the gain of the device. The loss in coupling from the focusing or defocusing effect results in lower gain. By choosing a better design for the undulator, this unwanted effect is reduced.

The field structure found from integration is used to determine the electron trajectories. The best design for the undulator is determined by the imposed input conditions on the electron beam for entry into the cavity. An additional benefit of this technique is in showing coil winding tolerances.

Several new simulation programs have been developed to calculate and graphically display the undulator magnetic fields. These calculations were used in new simulations for calculating the electron trajectories. This work resulted in two talks; one at the Twelfth International Free Electron Laser Conference in Paris, France and the other at the International Conference on Lasers '90 in San Diego, California. The talk in Paris has been submitted for publication in Nuclear Instruments and Methods in Physical Science, (1991). Additionally, a spread-sheet was started to display input and output parameters for comparison of different type FELs. The spread-sheet would be useful for a project manager in the Navy to determine optimum design parameters as a second check on proposals. This project will be completed by a following thesis student.

II. BACKGROUND

A. THEORY OF FREE ELECTRON LASERS

The Free Electron Laser has many of the same attributes as a regular laser. Some of these attributes are "...remarkable directionality, spectral purity, and intensity" [2]. An ordinary laser is composed of several components (Figure 1).
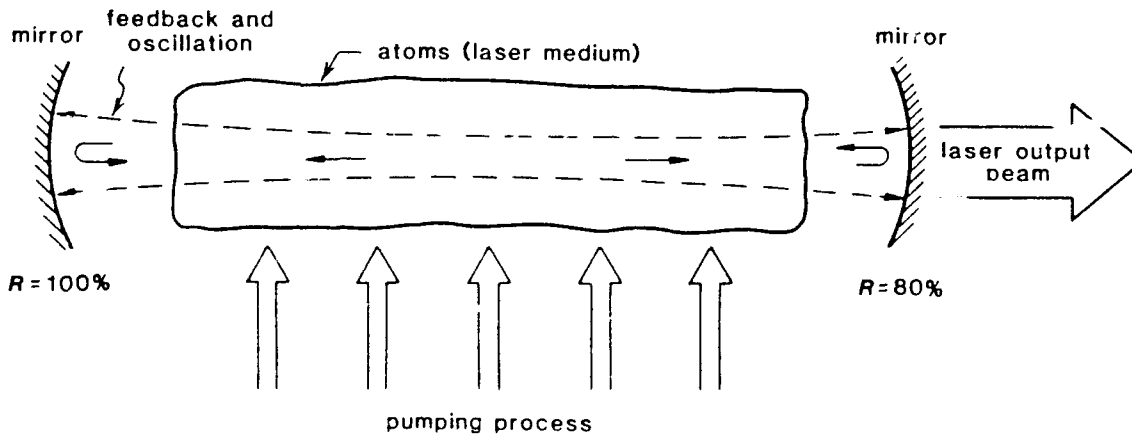
Figure 1 .

Elements of a typical laser from Ref. [2].

The essential elements of a laser are: (i) a lasing medium; (ii) a pumping process; and (iii) suitable optical feedback elements that allow a beam of radiation to either pass once through the laser medium (as in a laser amplifier) or bounce back and forth repeatedly through the laser medium (as in a laser oscillator) [2].

The Free Electron Laser is constructed differently (Figure 2) and uses different physics to evolve the light amplification. Figure 2 shows the overall components and the relationship between the electron trajectory and the co-propagating light. The FEL lasing medium is a relativistic electron beam. The FEL pumping process is from the energy exchange between the electron beam and co-propagating light in a vacuum. Mirrors form the optical feedback system shown for an oscillator configuration. The amplifier configuration does not have mirrors.

Figure 2 .

Schematic showing basic FEL setup. Also shown is the positional (phase) relationship between the light wave and the electron trajectory from Ref. [3].

One of the attributes that the FEL possesses is the capability to "tune" the output radiation over a range of wavelengths by changing the electron beam 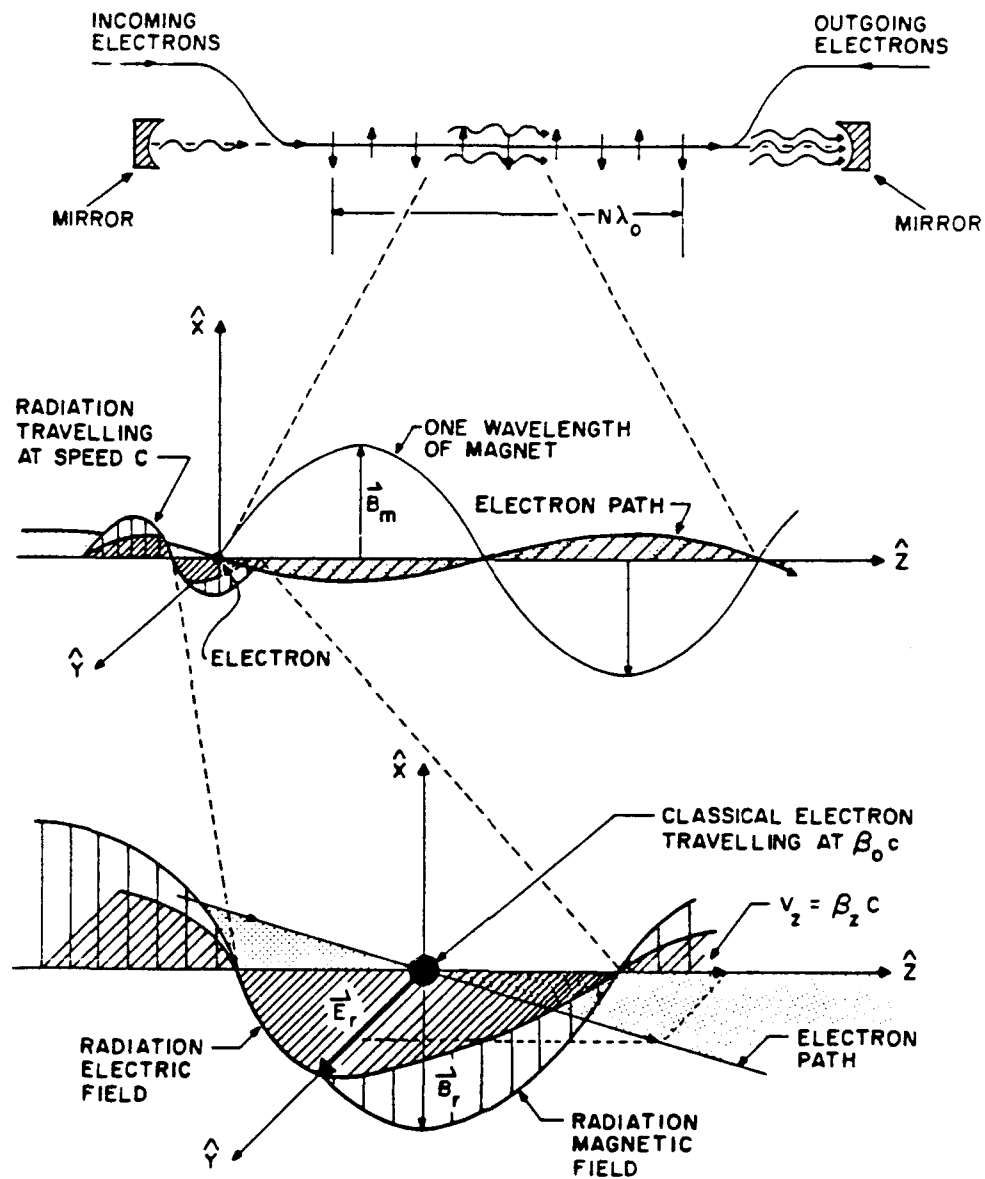or undulator parameters. Another attribute is the absence of extraneous material in the lasing medium, allowing the possibility for increasing the power density to weapons grade potential. Thus, the FEL is a candidate for a Directed Energy Weapon, and its tunability gives it flexibility in optimizing atmospheric propagation [1].

Given the description of an FEL made earlier, we need to understand the physics of the device. Upon entering the undulator, the relativistic electrons are "wiggled" back and forth by alternating magnetic fields. From electrodynamic theory, we know that a relativistic charged particle that is accelerating produces electromagnetic radiation in the forward direction. The radiation is emitted in a cone centered around the particle velocity that resembles a "flashlight" (Figure 3).

Figure 3 .

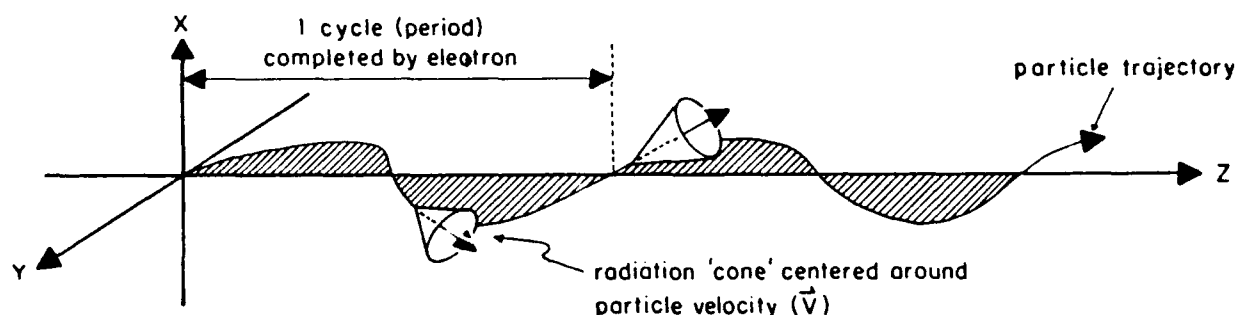Relativistic emission of radiation by an accelerating charged particle.

Since the width of cone is wide compared to the cavity dimensions, most of the radiation is lost and only 10% is retained. Subsequent electrons will radiate into the cavity also. Even though there is only about one photon radiated per pass per electron, the electron beam density is approximately 10^{12} electrons/cm^3 so that

there is a large photon density. Due to the resulting large photon density, spontaneous emission will rapidly be dominated by stimulated emission leading to coherence. Spontaneous emission is responsible for the self-starting capability of the FEL. As spontaneous emission is replaced by stimulated emission, the conditions are set to start matching the electron velocity vectors with the co-propagating radiation. This matching leads to energy transfer between the electrons and the light and is known as coupling. The coupling is responsible for the gain of the device. The high energy transfer and efficiency of the FEL comes from the coupling of the free electrons to the coherent radiation set up in the cavity.

To understand this coupling, we need to develop a few equations. Assume the radiation is established with a particular wavelength (Figure 4). The velocity of the electron is $\vec{v} = \vec{\beta}c$ where c is the speed of light. Since the electrons are relativistic, the transverse velocities are small with respect to the velocity in the z direction, $|\vec{\beta}| \approx \beta_z = v_z/c$. The period of the transverse electron motion corresponds to an undulator wavelength λ_o. The condition of _resonance_ occurs when the speed difference between the electron and the light is such that one wavelength of light, λ, passes over the electron as the electron travels through one undulator wavelength, λ_o. The electron travels through the undulator period of Figure 4 in the time interval $\Delta t = \lambda_o/(\beta_z c)$. Considering the difference in speeds, the condition of resonance describes the wavelength of light after the electron has traveled through an undulator period. At resonance, we find

$$\lambda = c\Delta t - \beta_z c\Delta t = c\Delta t - \lambda_o = (1 - \beta_z)\lambda_o/\beta_z \quad . \tag{1}$$

For relativistic electrons with small transverse velocity, the Lorentz factor is

$$\gamma = \frac{1}{\sqrt{1 - \frac{v^2}{c^2}}} \quad , \text{ but } \beta_o = \beta_z = \frac{v_z}{c} \quad \text{ so}, \quad \beta_z = (1 - \gamma^{-2})^{1/2} \quad . \tag{2}$$

7

Using the binomial theorem $(1 - x)^n = 1 - nx + (n/2)(n-1)x^2 - \cdots$, and neglecting second-order and higher terms, we arrive at

$$\beta_z = 1 - \frac{1}{2\gamma^2} \qquad . \tag{3}$$
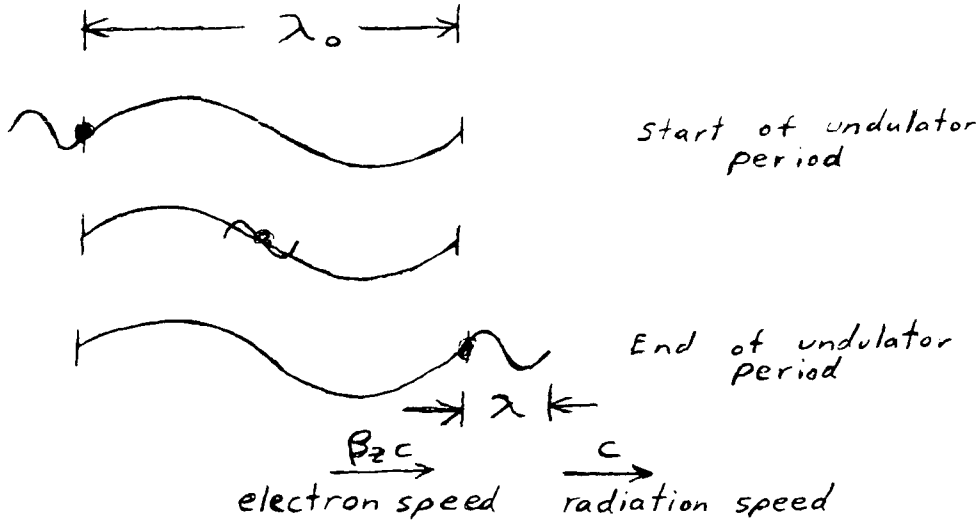
Figure 4 .

Schematic showing relative positions of the electron and light wave through an undulator period λ_o.

Using (3), we have

$$\lambda \simeq \frac{\lambda_o}{2\gamma^2} \qquad . \tag{4}$$

This is the relationship between the undulator wavelength, λ_o, the electron energy, γ, and the wavelength of light in the cavity, λ. If either γ, or λ_o, are changed, the wavelength of the cavity radiation, λ, is changed. This shows the tunability of the Free Electron Laser.

The preceding discussion shows some of the relationships between different parameters in the undulator. Figure 5 shows a planar representation of the relationship between the electron trajectory and the undulator field. We want to

8

find the equations of motion for the electron so we need to develop expressions for the forces and fields affecting it.

Figure 5 .

Simplified planar representation of one undulator
period and resultant electron trajectory.

The charged electron feels a force given by

$$\vec{F} = q(\vec{E} + \vec{v} \times \vec{B}) \quad , \tag{5}$$

where

$\vec{v}$ is the electron velocity,

$\vec{E}$ is the electric field felt by the electron,

q is the charge of the electron, and

$\vec{B}$ is the magnetic field felt by the electron.

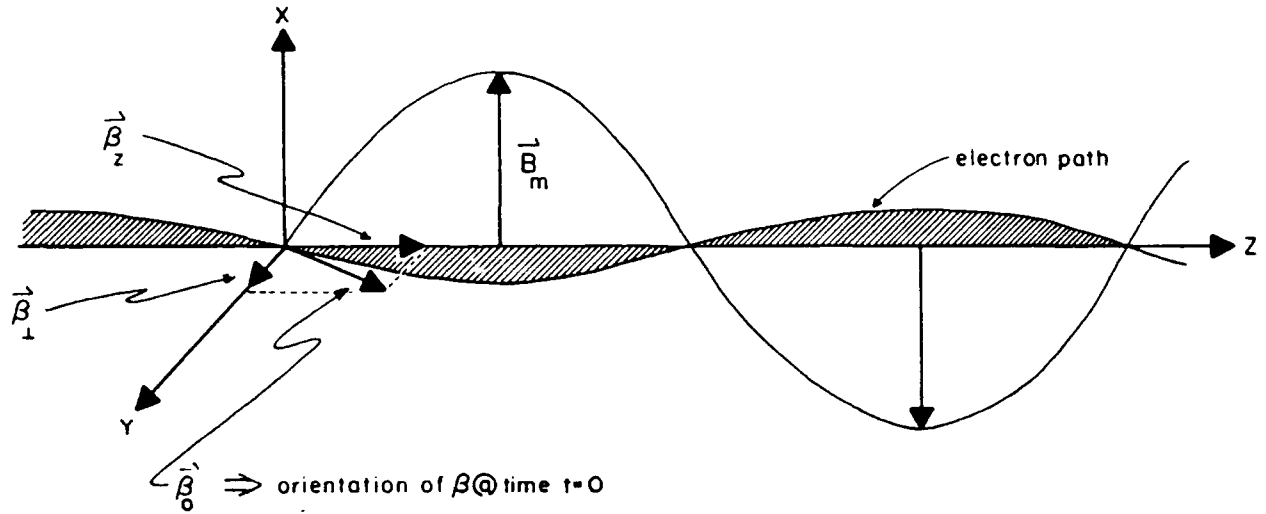The only fields felt by the electron are due to the cavity radiation, $\vec{E}_r$, and the total magnetic field which consists of the undulator magnetic field, $\vec{B}_m$ and the radiation magnetic field, $\vec{B}_r$. Therefore,

$$\vec{F} = \frac{d}{dt}(\gamma m \vec{v}) = \frac{d}{dt}(\gamma m \vec{\beta}c) = q(\vec{E}_r + \vec{\beta}c \times \vec{B})$$

$$\frac{d}{dt}(\gamma\vec{\beta}) = -\frac{e}{mc}[\vec{E}_r + \vec{\beta}c \times (\vec{B}_m + \vec{B}_r)] \quad . \tag{6}$$

Now, using the definition of momentum gives

$$\vec{F} = \frac{d\vec{p}}{dt} = mc\frac{d}{dt}(\gamma\vec{\beta}) \quad ,$$

but the electron energy is $E = \gamma mc^2$. The energy change is $dE/dt = \vec{F} \cdot \vec{v}$, so

$$\frac{dE}{dt} = mc^2\frac{d\gamma}{dt} = q(\vec{E}_r + \vec{\beta}c \times \vec{B}) \cdot \vec{v} = q\vec{E}_r \cdot \vec{\beta}c$$

$$\Rightarrow \quad \frac{d\gamma}{dt} = -\frac{e}{mc}(\vec{\beta} \cdot \vec{E}_r) \quad . \tag{7}$$

We now need expressions for the electric and magnetic fields. We want to relate the equations to our undulator design, so we choose helical polarization for the electric field to match the helical magnetic field undulator design selected. From basic optics, the generic forms for planar electric and magnetic radiation fields are [4],

$$\vec{E}_x(z,t) = E_x[\cos(kz - \omega t), 0, 0] \quad , \tag{8}$$

$$\vec{E}_y(z,t) = -E_y[0, \sin(kz - \omega t), 0] \quad , \tag{9}$$

where

$$|\vec{B}| = \frac{|\vec{E}|}{c} \quad , \quad k = \frac{\omega}{c} \quad ,$$

and ω = the angular frequency of the wave.

Circular polarization can be achieved by combining the planar forms with a spatial offset between them called a phase difference, ε. The waves move in the positive z

10

direction and combine to form a rotating E vector that describes a helix centered on the z axis as shown in Figure 6. If we put this in a combined form,

$$\vec{E} = E[\cos(kz - \omega t), -\sin(kz - \omega t), 0], \qquad (10)$$

it is easy to see that the magnitude of the electric field vector is constant, but the direction of the vector is a function of z and t.
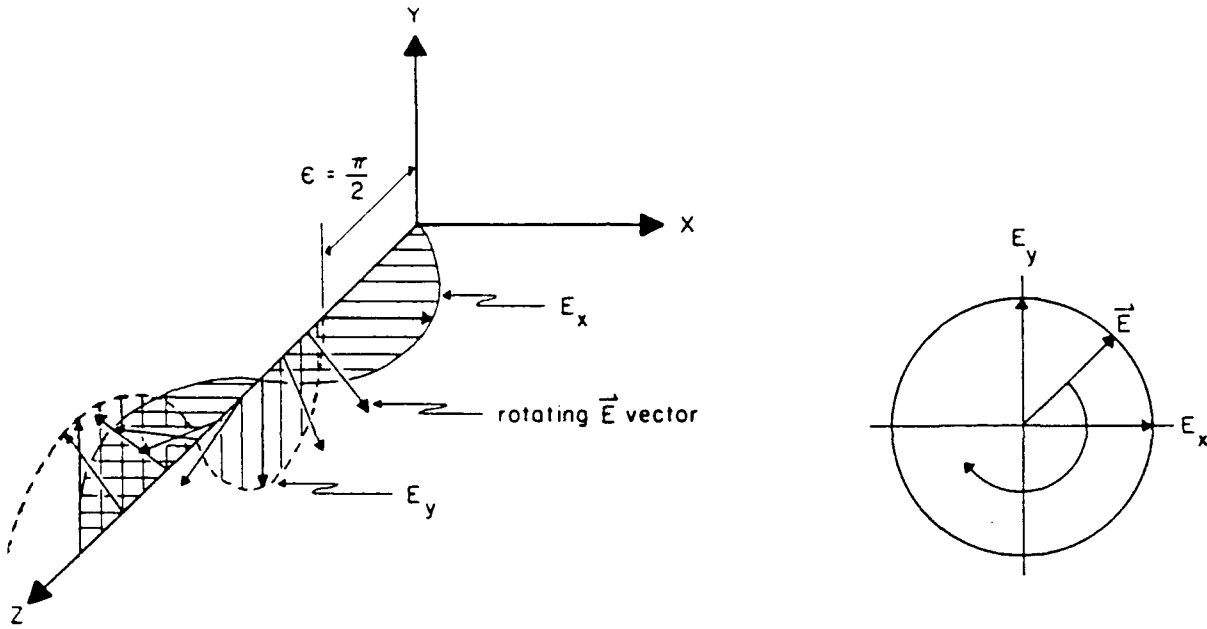
Figure 6 .

Construction of the total electric field vector ($\vec{E}$)

from the component forms. The rotating $\vec{E}$ describes

a circular helix along the z axis from Ref. [4].

If we set $\psi = (kz - \omega t)$, we can simplify the electric field vector to

$$\vec{E}_r = \vec{E}_x + \vec{E}_y = E[\cos(\psi), -\sin(\psi), 0]. \qquad (11)$$

11

Now that we know the form of the electric field, the magnetic field form can be deduced. To find $\vec{B}_r$, we use the required conditions for an electromagnetic wave that the electric and magnetic field vectors are perpendicular and their cross product points in the direction of the direction of propagation. Thus, we can set up the following schematic representation and find the orientation and thus the solution of the magnetic field vector (Figure 7).
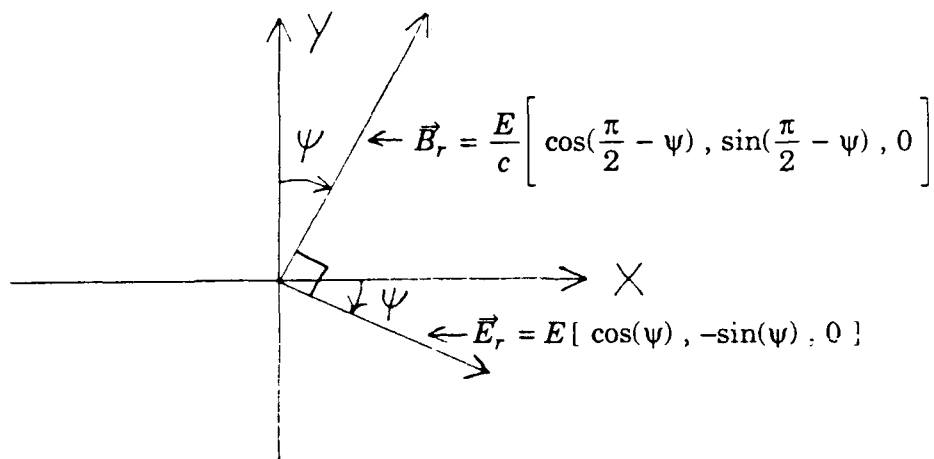
Figure 7 .

Schematic showing the orientation of the magnetic field vector,

$\vec{B}_r$, given the electric field vector, $\vec{E}_r$.

The equation for the magnetic field in Figure 7 was arrived at by using the form of the electric field and translating it to fit the conditions we just described. From geometry, we know that $\sin(\psi) = \cos(\pi/2 - \psi)$ and $\cos(\psi) = \sin(\pi/2 - \psi)$. Thus, the simplified form for the magnetic field becomes

$$\vec{B}_r = \frac{E}{c}[\sin(\psi), \cos(\psi), 0] . \tag{12}$$

12

The helical magnetic field has the form,

$$\vec{B}_m = B_m [\cos(k_o z) , \sin(k_o z) , 0] \quad , \tag{13}$$

$$\text{where} \quad k_o = 2\pi/\lambda_o \quad .$$

By substituting equations (11-13) for the fields into our equations of motion, we can arrive at the components of the Lorentz Force equation:

$$\frac{d}{dt}(\gamma \vec{\beta}_\perp) = -\frac{e}{mc}\left[E(1-\beta_z)(\cos \psi , -\sin \psi , 0) + \beta_z c B_m (-\sin k_o z , \cos k_o z , 0) \right] , \tag{14}$$

$$\frac{d}{dt}(\gamma \beta_z) = -\frac{e}{mc}\left[E(\beta_x \cos \psi - \beta_y \sin \psi) + c \beta_m (\beta_x \sin k_o z - \beta_y \cos k_o z) \right] , \tag{15}$$

$$\frac{d\gamma}{dt} = -\frac{e}{mc}[\beta_x \cos \psi - \beta_y \sin \psi] \quad . \tag{16}$$

In the equations above, the large scale motion is $\vec{\beta} = \beta_z \hat{z}$. The next largest scale motion is the transverse "wiggling" motion, $\beta_\perp$. For relativistic electrons, $\beta_z \to 1$, so $(1 - \beta_z) \to 0$, and we eliminate the first term of (14) above.

By integrating (14), the transverse velocity ratio $\vec{\beta}_\perp$ is found to be

$$\vec{\beta}_\perp = -\frac{K}{\gamma}[\cos(k_o z) , \sin(k_o z) , 0] \quad , \tag{17}$$

where $K = eB_m \lambda_o /(2\pi mc)$. We insert (17) in the relation for the energy change, (16), to get

$$\dot{\gamma} = \frac{eKE}{mc\gamma} \cos(\zeta) \quad , \tag{18}$$

where $\zeta = (k + k_o)z - \omega t$.

If we take a closer look at the electron phase, ζ, we see that the important factor is the position of the electron. At the beginning of the undulator, time t = 0, $\zeta(0) = \zeta_o = (k + k_o)z_o = 2\pi z_o/\lambda$, since $k \gg k_o$. Thus, the electron phase, ζ, is a "microscopic" variable in that it scales with the optical wavelength. We can relate the value of ζ to energy exchange between the electron and the light wave. We can see that the physics of the energy exchange is proportional to $\cos(\zeta)$, and

13

$-1 \leq \cos(\zeta) \leq 1$. The initial electron phases, ζ_o, are random with respect to the light wave, and thus, form a uniform distribution of phases. Therefore, half of the electron phases, ζ_o, are such that $\dot{\gamma} > 0$, and half are such that $\dot{\gamma} < 0$. We need a better way to express the energy exchange, because it looks like we're not going to get $\underline{any}$ energy exchange from (18)! Lets try relating $\dot{\gamma}$ and $\ddot{\zeta}$ to complete the feedback loop. From (2), we have

$$\frac{1}{\gamma^2} = 1 - (\vec{\beta}_z + \vec{\beta}_\perp)^2 = 1 - \beta_z^2 - \beta_\perp^2 \quad ,$$

but using (17), we find that $\beta_\perp^2 = K^2/\gamma^2$. Therefore, $\beta_z^2 = 1 - (1 + K^2)/\gamma^2$. By taking the time derivative and some algebraic manipulation, we can find that for $\gamma \gg 1$,

$$\dot{\gamma} = \frac{\gamma^2}{1 + K^2} \frac{\gamma \ddot{\zeta}}{(k + k_o)c} = \frac{\gamma^2}{1 + K^2} \frac{\gamma \ddot{\zeta}}{kc} \qquad \text{since} \quad k \gg k_o \quad . \tag{19}$$

To get this in a better form, it can be shown that by using (3), and the relation $\beta_z^2 = 1 - (1 + K^2)/\gamma^2$,

$$\lambda \simeq \frac{\lambda_o}{2\gamma^2}(1 + K^2) \quad , \tag{20}$$

which is a more accurate expression describing FEL resonance than (4)! By inserting (20) into (19), we find that

$$\dot{\gamma} = \frac{eKE}{\gamma mc}\cos(\zeta) = \frac{\gamma \ddot{\zeta}}{2\omega_o} \quad .$$

Substituting into (18), we have

$$\ddot{\zeta} = \frac{2eKE\,\omega_o}{\gamma^2 mc}\cos(\zeta) \quad . \tag{21}$$

This expression can be made more meaningful by defining a dimensionless time τ, where $\tau = \beta_o ct/L = ct/L$. The dimensionless time has the values $0 \leq \tau \leq 1$ along the undulator length L. We define τ because the total time spent in the

14

undulator is about $L/c \simeq 10^{-8}$ seconds for a typical undulator. Using the definition of τ above, we have

$$d\tau^2 = \frac{c^2}{L^2}dt^2 \qquad \text{and} \qquad (\overset{\circ\circ}{\ }) = \frac{d^2(\ )}{d\tau^2} \quad .$$

Expression (21) can be simplified to the pendulum equation,

$$\overset{\circ\circ}{\zeta} = |a|\cos(\zeta) \quad , \tag{22}$$

$$\text{where} \quad |a| = \frac{4\pi eKNLE}{\gamma^2 mc^2} \quad .$$

Specifically,

$\overset{\circ\circ}{\zeta}$ = phase acceleration of the electron,

$\overset{\circ}{\zeta} = v$ = phase velocity of the electron,

ζ = phase of the electron, and

$|a|$ = optical field amplitude.

We also know that $\overset{.}{\zeta} = (k + k_o)\dot{z} - \omega$ implying that $\overset{\circ}{\zeta} = L[(k + k_o)\beta_z - k]$. Now we have a relationship between the phase ζ, and the phase velocity, v.

The phase and phase velocity can be plotted on a phase space plot that shows the evolution of the electron trajectories in phase space. The path separating open and closed orbits in phase space is called the "separatrix",

$$v_s^2 = 2|a|[1 + \sin(\zeta_s + \phi)] \quad , \tag{23}$$

where ϕ is the optical phase. The separatrix passes through the fixed points $(-\pi/2, 0)$ and $(3\pi/2, 0)$. The peak-to-peak height of the separatrix is $4|a|^{1/2}$, while the horizontal position is determined by the optical phase (Figures 8 and 9). The electrons are injected into the undulator and therefore start their phase space orbits with initial phase, ζ_o, and initial phase velocity, v_o. How well the electron distribution is arranged on the phase space picture is a direct indication of the beam quality. The poorer the beam quality, the broader the distribution will be.
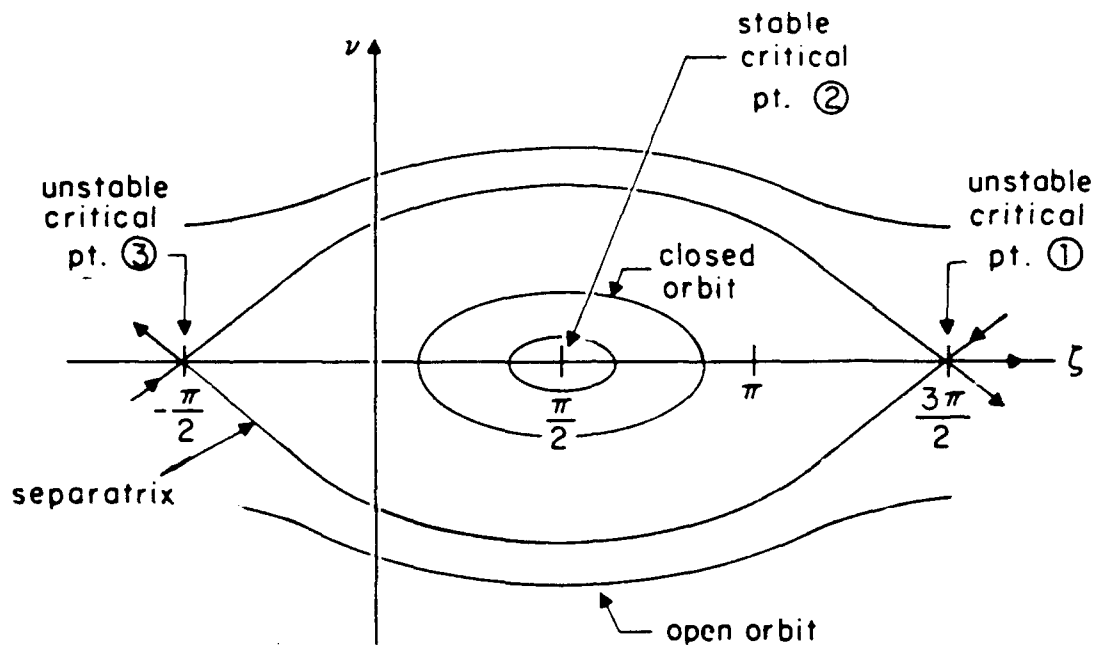
15

Figure 8 .

Phase space plot of electron phase vs. phase velocity.
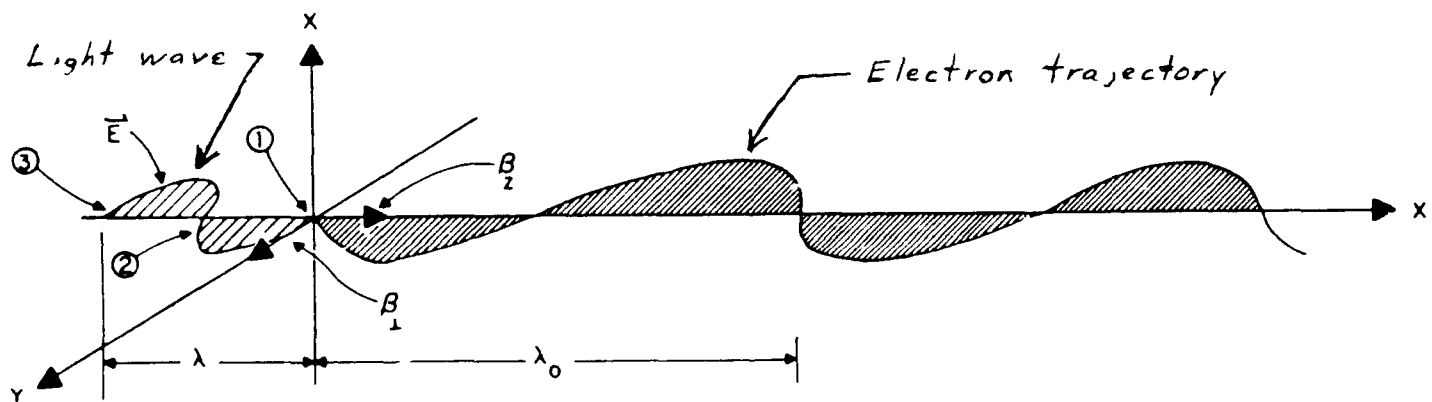
Figure 9 .

Schematic of the phase relationship between the electron

trajectory and the light wave.

Figure 8 is a plot of phase space that shows graphically the relationship we have just developed. Figure 9 is a plot of the relative positions of the light, and the electron path as the phase space plot cycle begins. The numbers show possible relative positions between the light and the electron as they enter the undulator. The correspondence between the numbers in Figure 8 and Figure 9 are:

Point 1 (relative phase position shown) is an unstable critical point.

Point 2 (if it were at the origin in Fig. 9) corresponds to a stable
   critical point.

Point 3 (if it were at the origin in Fig. 9) describes the same condition
   as point 1.

The gain of the FEL comes from a bunching of the electrons as they interact with the light that is best depicted in phase space. As seen in Figure 10, the electrons in the left hand side of the separatrix have gained in phase velocity (absorbed energy from the light) and the electrons in the right hand side have lost in phase velocity (lost energy to the light).
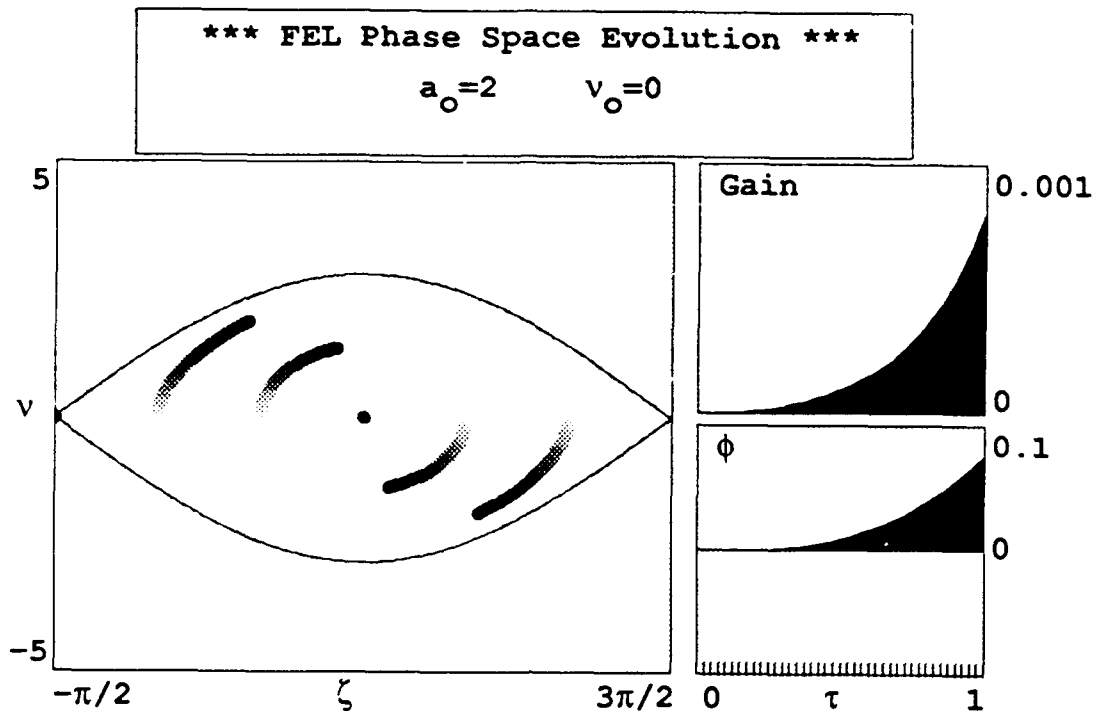
Figure 10 .

Phase space plot for electrons injected in the resonance condition.

If the electrons are allowed to continue the interaction for a longer time, the motion will continue. Some electrons lose energy and some gain, so that there is no net energy transfer and the gain is zero. If the electrons are given a non-zero initial phase velocity, there is a difference in the net energy exchange and non-zero gain is achieved (Figure 11). It can be shown that the maximum gain is achieved at $v_o = 2.6$.

18
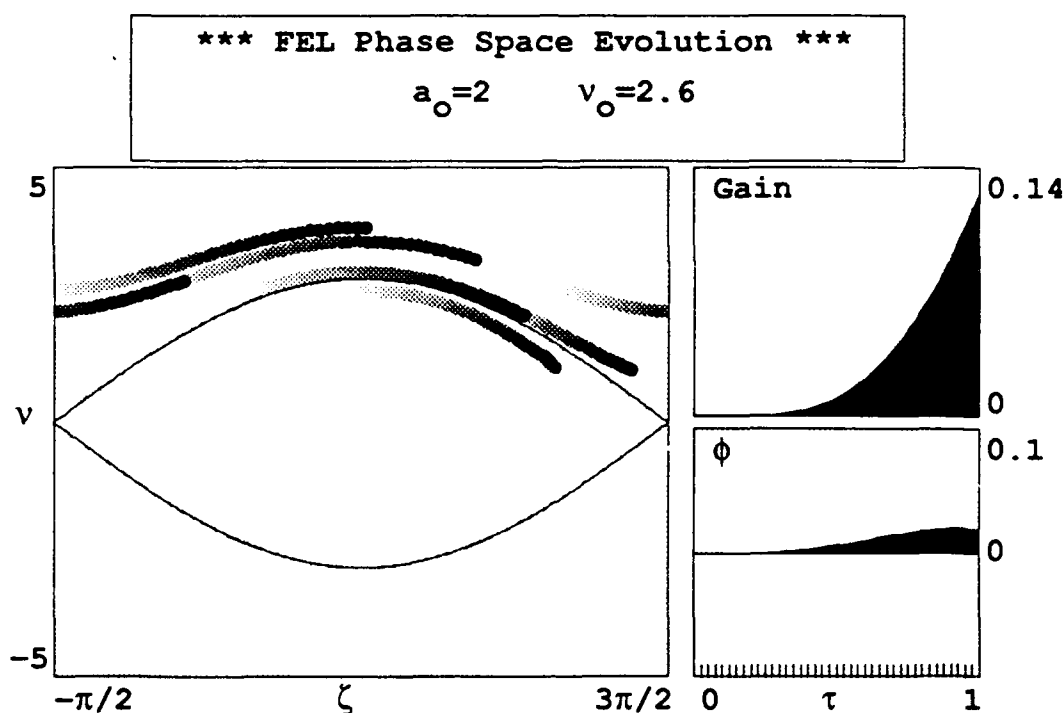
Figure 11 .

Phase space plot for electrons injected with a positive initial phase velocity.

The proceeding discussion shows that the electron positions and velocities are critical to the performance of the FEL. If the initial electron velocities are random over a significant range, bunching of the electrons degrades and the gain is small. If non-uniform magnetic fields cause deflections from the undulator axis, the electron phase velocities are changed, bunching can be destroyed and the gain is small. Thus, the FEL undulator, which controls the magnetic field magnitude, length of interaction and uniformity of fields, is critical to the ultimate performance of the device. It is easy to see that optimization of undulator design is crucial to all applications of the Free Electron Laser.

19

B. UNDULATOR DESIGN

Many Free Electron Lasers have been built incorporating various attributes. As in most endeavours, there is no one design that has all desirable traits incorporated. Thus, the researcher must decide which specific parameters are most important and design the optimum device to achieve it. There are two general classes of undulators available today. They are the linearly polarized and the circularly polarized classes. The linearly polarized class primarily uses permanent magnet structures while the circularly polarized undulator primarily uses current carrying coils to establish the magnetic fields.

1. Linearly polarized undulator

The permanent magnet structures produce a linearly polarized magnetic field of the form [5],

$$\vec{B}^L = B_m [\, 0 \,,\, \sin(k_o z)\cosh(k_o y) \,,\, \cos(k_o z)\sinh(k_o y) \,] \;. \tag{24}$$

The perfect electron trajectories are sinusoidal in the y-z plane with no motion in the x direction. Away from the undulator axis, the average transverse field strength increases in the x direction only,

$$\bar{B}_\perp^L = \frac{B_m}{\sqrt{2}} \left[\, 1 + \frac{k_o^2 x^2}{2} + \cdots \,\right] \;. \tag{25}$$

This undulator provides focusing in the x direction, but not in the y direction. In practice, the experimenter uses other forms of magnetic focusing, such as a quadrupole lens or machining a slight parabolic curve in the normally flat magnet pole faces. The curved surface produces a smaller gap between the magnetic poles off axis, thus increasing the field strength off axis. The parabolic shape results in equal focusing in each radial dimension to maintain a circular electron beam cross section. The field from parabolic pole design with equal x-y focusing is

20

$$B_x^L = B_m \sinh\left[\frac{k_o x}{\sqrt{2}}\right] \sinh\left[\frac{k_o y}{\sqrt{2}}\right] \cos(k_o z) \quad , \quad B_y^L = B_m \cosh\left[\frac{k_o x}{\sqrt{2}}\right] \cosh\left[\frac{k_o y}{\sqrt{2}}\right] \cos(k_o z) \quad ,$$

$$B_z^L = -2B_m \cosh\left[\frac{k_o x}{\sqrt{2}}\right] \sinh\left[\frac{k_o y}{\sqrt{2}}\right] \sin(k_o z) \quad . \tag{26}$$

The perfect electron trajectories on the axis are again sinusoidal in the y-z plane, but away from the axis the transverse field increases in both the x and y direction equally,

$$B_\perp^L = \frac{B_m}{\sqrt{2}}\left[1 + \frac{k_o^2(x^2 + y^2)}{4} + \cdots\right] \quad . \tag{27}$$

Notice that the magnitude of the average field seen by the electrons on axis is $\bar{B}_\perp^L = B_m/\sqrt{2}$. The average transverse acceleration of the electrons is smaller due to the magnetic field reduction, and thus, the linear undulator gain is reduced. As we will see, this is not a problem with the helical undulator, but the construction techniques involved make the linear undulator much less complicated to build.

2. Circularly Polarized Undulator

The helical undulator with circular polarization has a field involving first-order Bessel functions, but near-axis fields can be approximated with error <1% , for $k_o r < 0.8$ by [5,6]

$$B_x^H = -B_m\left[\left[1 + \frac{1}{8}k_o^2(3x^2 + y^2)\right]\sin(k_o z) - \left[\frac{1}{4}k_o^2 xy\right]\cos(k_o z)\right] \quad ,$$

$$B_y^H = B_m\left[\left[1 + \frac{1}{8}k_o^2(x^2 + 3y^2)\right]\cos(k_o z) - \left[\frac{1}{4}k_o^2 xy\right]\sin(k_o z)\right] \quad , \quad \text{and}$$

$$B_z^H = -B_m k_o\left[1 + \frac{1}{8}k_o^2(x^2 + y^2)\right][x\cos(k_o z) + y\sin(k_o z)] \quad . \tag{28}$$

Electrons injected into these fields will travel in helical paths centered along the z axis. Comparing the average transverse magnetic fields, we find that

$$\mathcal{B}_{\perp}^{H} = B_m \left[1 + \frac{k_o^2 r^2}{4} + \cdots \right] , \tag{29}$$

and it is easy to see that off-axis fields are stronger closer to windings. This radial increase of the fields has a "focusing" effect on the electrons which results in a slow oscillation around the longitudinal axis. This motion is known as Betatron oscillations. The magnitude of the average field seen by the electrons on axis is $\mathcal{B}_{\perp}^{H} = B_m$ which results in higher transverse acceleration of the electrons. This in turn causes greater electron bunching, and thus, higher gain.

Greater coupling and simplicity led us to choose the helical bifilar design. With this design in mind, another attribute we desire is a shorter wavelength light output. One of the ways to accomplish this is the electromagnetic compact FEL.

C. THE COMPACT FEL

The compact FEL design is one method of accomplishing shorter wavelength light output. Since we know that

$$\lambda = \frac{\lambda_o}{2\gamma^2} (1 + K^2) , \tag{30}$$

by shortening the length of our undulator period, we can shorten the light wavelength. Shorter wavelength light has many desirable properties such as atmospheric window propagation, and laboratory material interaction to name just a few. Shorter wavelength light also has higher energy so energy deposition on targets is greater. Thus, the compact bifilar helix is the design chosen to illustrate our modeling technique.

1. Specifications

Originally proposed by Roger Warren (LANL) [7], and considered as a tentative experiment for LANL and the Naval Postgraduate School, the following parameters were used:

22

Number of periods N = 10 ,

Undulator period λ_o = 0.9cm ,

Gap $2g$ = 4mm , and

Lorentz factor γ = 30.35 .

Although this is the basis of comparison throughout this paper, all lengths were non-dimensionalized by dividing by λ_o for ease of transposition to other undulator designs.

2. Winding schemes

Using the dimensions for the proposed compact FEL, it is easy to see that the windings of the bifilar helix cannot be of a complicated nature. The small dimensions make the winding terminations at both ends of the undulator, and the method of power lead connection extremely important to the resultant magnetic field structure at the entrance to the undulator. We will see that the lead wires at the end of the undulator carry sufficient current to cause unwanted perturbations in the incoming electron beam.

Three terminations are investigated in this paper: the wire, loop and staggered termination schemes [8]. In the case of wire termination, the bifilar helical wires are continued radially outward when they reach the end of the undulator as shown in Figure 12a. In the case of loop termination, a circle of wire is attached to the end of the cylinder formed by the helix with the windings attached at opposite positions on the circle. Thus, the current from one helical winding enters at one position on the circle, flows equally around each side of the circle, and then combines to flow in the opposite direction in the opposing helical winding as shown in Figure 12b. Staggered terminations are achieved by using wire or loop terminations as a current taper for the undulator removing a specified percentage of the current per termination depending on its position in front of an

extended undulator. This is visualized by extending the bifilar helix windings past the entrance to the undulator, and connecting them periodically by a termination which passes a percentage of the current in the helical windings. Thus, the current flowing in the helical windings is reduced stepwise by the number of terminations added prior to the entrance of the undulator. This results in a tapering of the magnetic field. Tapering of the magnetic field at the entrance of the undulator can also be achieved by flaring the windings which is accomplished by using a progressively larger radius for the extended bifilar windings as distance before the original undulator entrance increases. The Loop termination scheme with current tapering (staggering) vice flaring the windings results in the smallest magnetic field spike at the entrance of the undulator [8]. This paper investigates fields at the entrance of the undulator in the compact FEL. The effect of undulator exit termination is explored as well, and the fields found are used to determine the incoming electron trajectories.
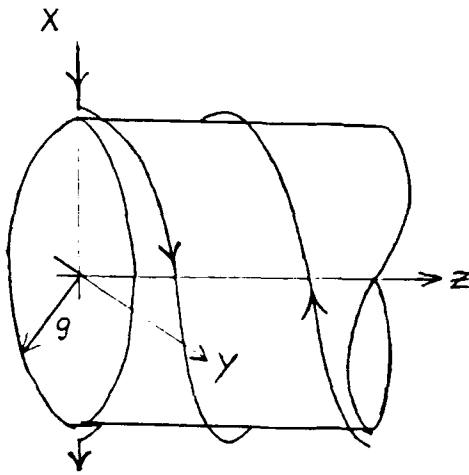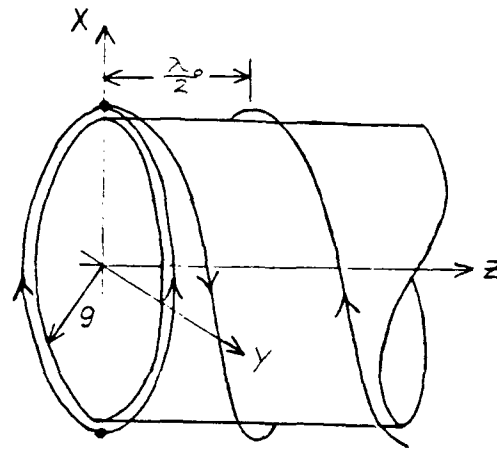
(a)   (b)

Figure 12 .

Illustrations of termination geometry for (a), Wire termination

and (b), Loop te mination.

III. MODELING OF UNDULATOR CHARACTERISTICS

A. REPRESENTATION OF FIELDS

1. Theory

As discussed in the background section, this paper calculates the magnetic field at any point by using the Biot-Savart law. The magnetic field at any position can be expressed by,

$$\Delta \vec{B} = \frac{\mu_o I}{4\pi} \frac{\Delta \vec{L} \times \vec{r}}{r^3} , \tag{31}$$

$$\text{where} \quad r = [\, r_x^2 + r_y^2 + r_z^2 \,]^{1/2} .$$

$\Delta \vec{B}$ is the magnetic field contribution at the desired position by th current element. μ_o is the magnetic permeability constant. I is the current flowing in the current element, $\Delta \vec{L}$. The distance and direction of the desired position from the current element is expressed by $\vec{r}$. By integrating over the winding configuration of choice, the magnetic field at any particular position can be found. To find the current elements, $\Delta \vec{L}$, we need to investigate the particular geometry of our winding configuration.

a. Integration of Magnetic Field

To develop the integration, we describe a very small piece of a current carrying wire in a particular geometry. As discussed previously, the methods of termination discussed will be; (i) Wire, (ii) Loop, and (iii) application of

wire and loop to the exit configuration. First, we need to discuss the geometry of the helical windings to set up the periodic magnetic field needed for undulator operation (Figure 13).
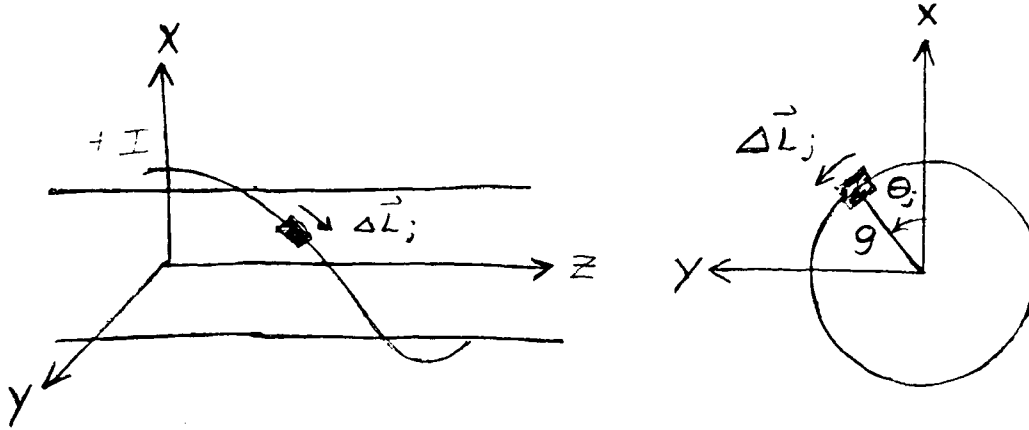
Figure 13 .

Schematic representation of the bifilar helical path.

(1) Helical Windings. Referring to Figure 13, we can represent the position and angle of the current element by

$$x_j = g\cos\theta_j \quad , \quad y_j = g\sin\theta_j \quad , \quad z_j = \frac{j}{n_z} \quad ,$$

where $\quad \theta_j = \dfrac{2\pi j}{n_z} \quad , \quad j = 0, 1, 2, ..., Nn_z - 1 \quad ,$

n_z = No. of divisions of an undulator period, and

N is the number of periods in the undulator .

The current elements have the form:

$$\Delta L_x = \frac{-2\pi g\sin\theta_j}{n_z} \quad , \quad \Delta L_y = \frac{2\pi g\cos\theta_j}{n_z} \quad , \quad \Delta L_z = \frac{1}{n_z} \quad ,$$

27

where g = radius of the undulator.

Now use the definitions

$$\Delta L = (\Delta L_x^2 + \Delta L_y^2 + \Delta L_z^2)^{1/2} \quad , \quad \text{and}$$

$$r_x^2 = (x - x_j)^2 \quad , \quad r_y^2 = (y - y_j)^2 \quad , \quad r_z^2 = (z - z_j)^2 \quad ,$$

where (x, y, z) is the position of the electron,

to substitute into (31) to sum up all the contributions from the current elements in the helical windings. If we did not have to worry about end effects, this method would give the desired solution to the interior magnetic fields of the undulator. Unfortunately, this is not an infinite length undulator and we next start discussing the termination methods. The simplest method of termination and simulating the leads connected to a power supply is the wire termination method (Figure 14).
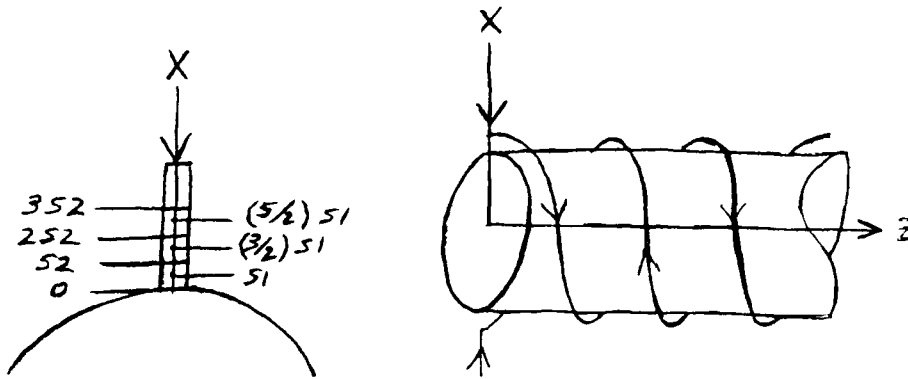
$$s1 = \frac{\pi g}{n_z} \qquad s2 = \frac{2\pi g}{n_z}$$

Figure 14 .

Schematic representation of the wire termination method.

28

(2) Wire Termination. Referring to Figure 14, we can describe the position and angle of the current element mathematically by,

$$x_e = a + e\left[\frac{2\pi g}{n_z}\right] - \frac{\pi g}{n_z} \quad , \quad y_e = 0 \quad , \quad z_e = 0 \quad ,$$

$$\text{where} \quad e = 1, 2, \cdots, 7n_z \ .$$

The current elements have the form:

$$\Delta L_x = \frac{-2\pi g}{n_z} \quad , \quad \Delta L_y = 0 \quad , \quad \Delta L_z = 0 \ .$$

The contribution of the wire termination is summed by substituting into (31) as explained for the helical windings. The top and bottom wires need to be differentiated in their individual contribution. The current elements in both produce the same respective orientation but the distance from the current element to the electron is different according to the following:

$$\text{Topwire}: \quad r_e = [\ (x - x_e)^2 + y^2 + z^2\ ]^{1/2} \quad ,$$

$$\text{Bottomwire}: \quad r_e = [\ (x + x_e)^2 + y^2 + z^2\ ]^{1/2} \quad .$$

As will be seen, this method of termination is by no means ideal. The other method of termination explored in this paper is loop termination (Figure 15).

29
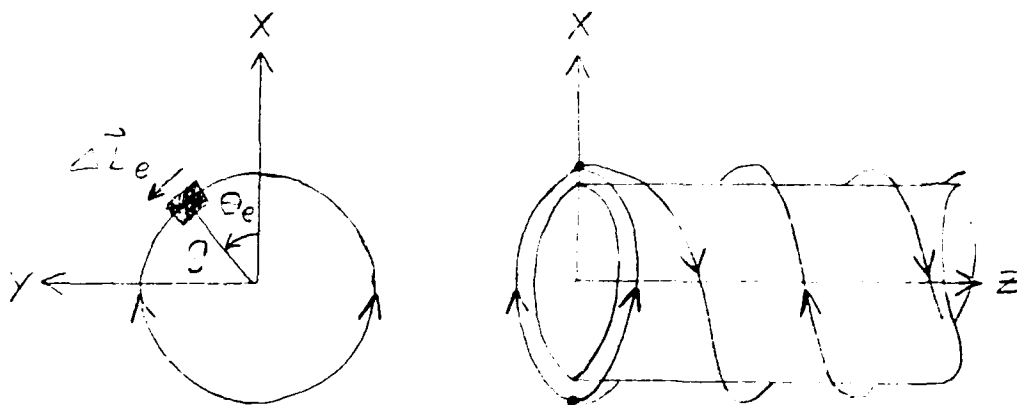
Figure 15 .

Schematic representation of the loop termination method.

(3) Loop Termination. Referring to Figure 15, we can describe the position and angle of the current element mathematically by,

$$x_e = g\cos\theta_e \quad , \quad y_e = g\sin\theta_e \quad , \quad z_e = 0 \quad ,$$

where $\quad \theta_e = \dfrac{2\pi e}{n_z} \quad$ and $\quad e = 0, 1, 2, ..., n_z \quad .$

The current elements have the form:

$$\theta_e = 0 \to 180^o: \quad \Delta L_x = \frac{2\pi g \sin\theta_e}{n_z} \quad , \quad \Delta L_y = \frac{-2\pi g \cos\theta_e}{n_z} \quad , \quad \Delta L_z = 0 \ .$$

$$\theta_e = 180 \to 360^o: \quad \Delta L_x = \frac{-2\pi g \sin\theta_e}{n_z} \quad , \quad \Delta L_y = \frac{2\pi g \cos\theta_e}{n_z} \quad , \quad \Delta L_z = 0 \ .$$

The current elements are summed as before. The last termination investigated is applying the wire and loop terminations to the exit of the undulator.

(4) Exit Termination. To apply wire termination to the end of the undulator, the only difference in the previous argument is to reverse the sign of the current flowing in the current elements. To apply loop termination to the exit, and still connect the power leads, requires close examination of the geometry (Figure 16).
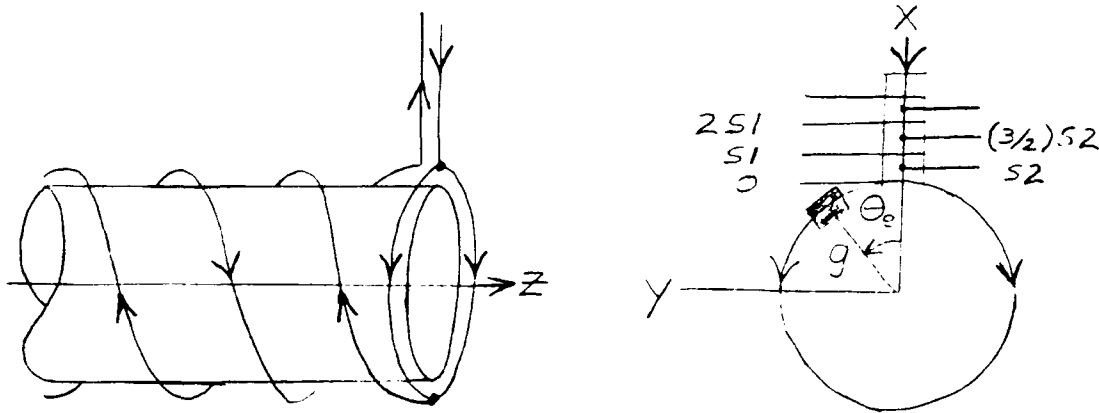
Figure 16 .

Schematic representation of loop termination at the exit (up).

As can be seen in Figure 16, the current in the loop exit termination is in the opposite direction. Also, replace all uses of z in the equations with $z - N$ to get the correct distance to the electron. The wire termination used to attach the power lead to the loop is a modification of the previous geometry using $z - N$ and the distance now becomes,

$$r_e = [(x - x_e)^2 + (z - N)^2]^{1/2} .$$

The wire termination used at the end of the second wire from the bifilar helix is the same as above except the current is reversed and the z distance becomes $z - 0.999N$ for physical separation of the leads.

31

The final variation studied is the exit termination with the wire connections going down (Figure 17).
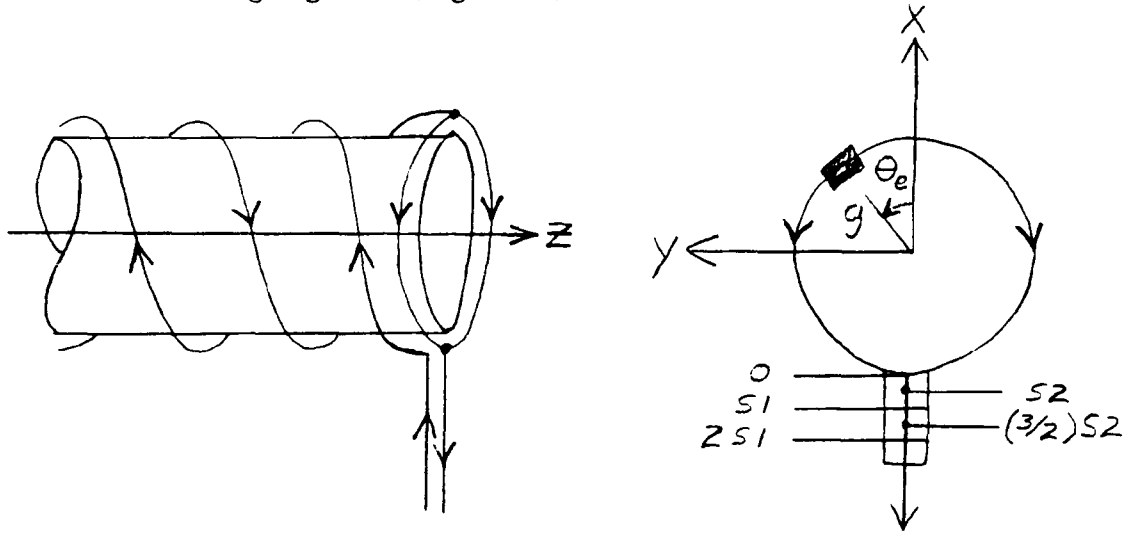
Figure 17 .

Schematic representation of loop termination at the exit (down).

The only variation in the equations from the previous discussion is in the r_x term. Replacing the minus sign with a plus sign achieves the necessary modification.

(5) Coil Winding Tolerances. Though not pursued in this paper, there is another possible application of the integration method discussed above. The flexibility of the current element integration technique allows easy change of the winding configuration. This flexibility would apply just as easily to displacing the windings slightly from the ideal positions explored. This would result in the ability to compare simulations to determine coil winding tolerances. The usefullness of this would help in the construction of actual undulators as outlined in [9].

b. Use of the K vector

The magnetic field at any point in the undulator is found from (31). A more useful quantity in the derivation used for the electron trajectories is the value K. Since the definition for K is $K = eB_m\lambda_o/(2\pi mc)$, we see that the value of K is proportional to B. Thus, the representations of the magnetic field shown will be using K to lead into the electron trajectory discussion.

2. Results

Now that we have developed the theory, we need to have some method of displaying the fields so we can get a better understanding of the stray field problem. As mentioned earlier, the Biot-Savart law was used to calculate the field contributions due to individual current elements. The field near the axis can be found analytically from (28) and agreed with the numerical calculations. Thus, the accuracy of the model is good, and can be applied to positions outside the undulator. The integration method also allows us flexibility in the winding configuration used for the integration. Thus, we can model the stray fields at the entrance to the undulator with the various termination schemes already discussed. The integration technique is first used to find the magnitude of the K vector along the axis for comparison between winding configurations, and as a comparison to the original work by Fajans [8]. In all simulations, the undulator entrance is fixed at z = 0. If tapering is used, it is added prior to this point making the undulator longer.

a. K Components

The first simulation is the K values for wire entrance and exit terminations. This will be referred to as wire/wire termination. This is the simplest of the termination techniques explored. The method of display is a dual plot of the x and y components of the K vector along the z axis. The z scale shows

the tapering used by a circle whose radius is proportional to the current centered on the undulator periods (Figure 18).

There is a slight asymmetry to the magnitudes of the two components as seen in the maximum and minimum values displayed. Notice that the y component of the K vector has a significant value for a considerable dis nce before z = 0. This is expected as the wires oriented for the termination contribute a field on axis in the y direction only. There is no large field gradient or spike at the entrance as predicted by Fajans [8]. The distance over which the y component can affect the entering electron trajectory may result in the same deflection as a large field spike.

** K magnitude for wire/wire terminations **

Kxmax=1.04   Kymax=1.28
N=10   Kxmin=-1.05   Kymin=-1.00
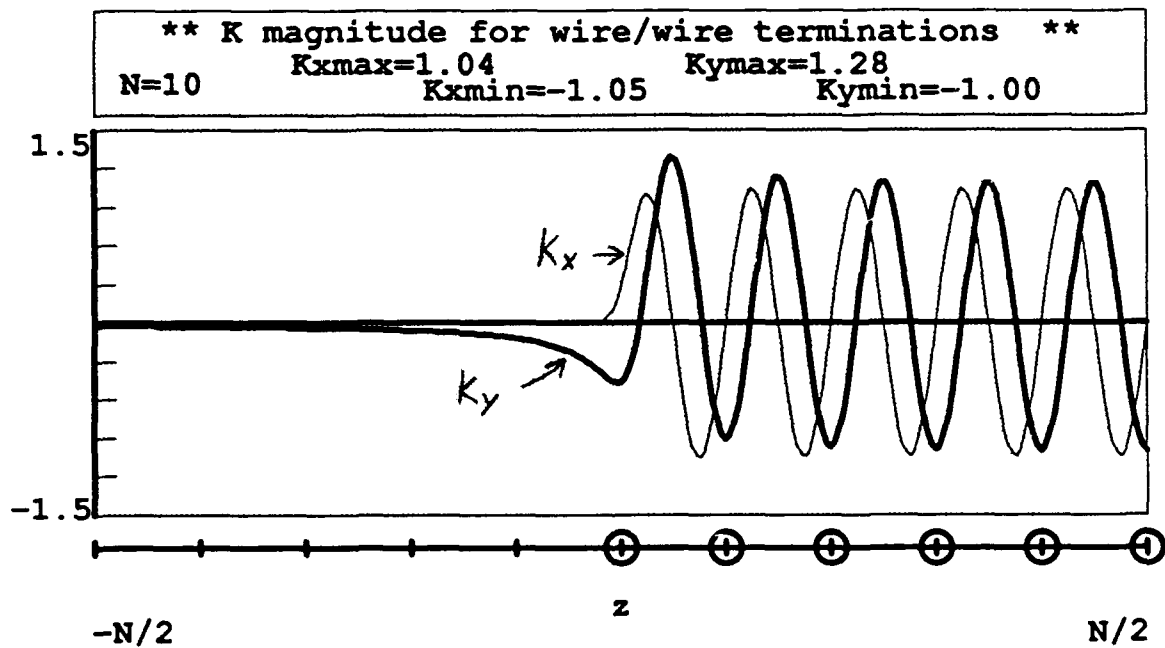
Figure 18 .

Combined plot of the K components along the z axis with no taper.

34

Also, there is an abrupt transition in the magnitude of the fields, especially in the x plane, right at the entrance to the undulator. To reduce the abrupt change, we try tapering the undulator. The first example of tapering uses a 1 period taper shown in Figure 19.
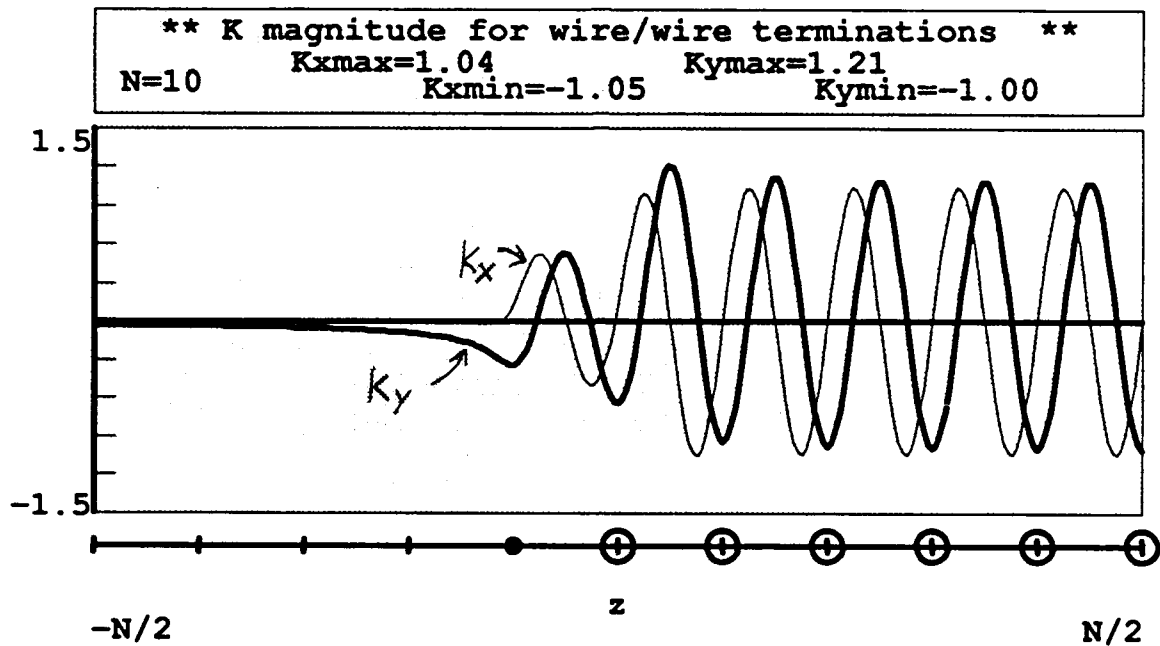
Figure 19 .

Combined plot of the K components along the z axis with 1 period taper.

As is seen, tapering ameliorates the abrupt field changes at the entrance. Unfortunately, the long lead of the y component is still evident. Also, even though tapering has been applied, there is a significant asymmetry still evident just inside the entrance.

This effect does not go away, even if the tapering is increased as shown in Figure 20. Like before, the long tail and asymmetric spike just inside the entrance is seen. The asymmetry of this termination scheme leads us to the suspicion that this winding design might not prove to be optimum.

** K magnitude for wire/wire terminations **
N=10   Kxmax=1.04   Kymax=1.17
        Kxmin=-1.05   Kymin=-1.00
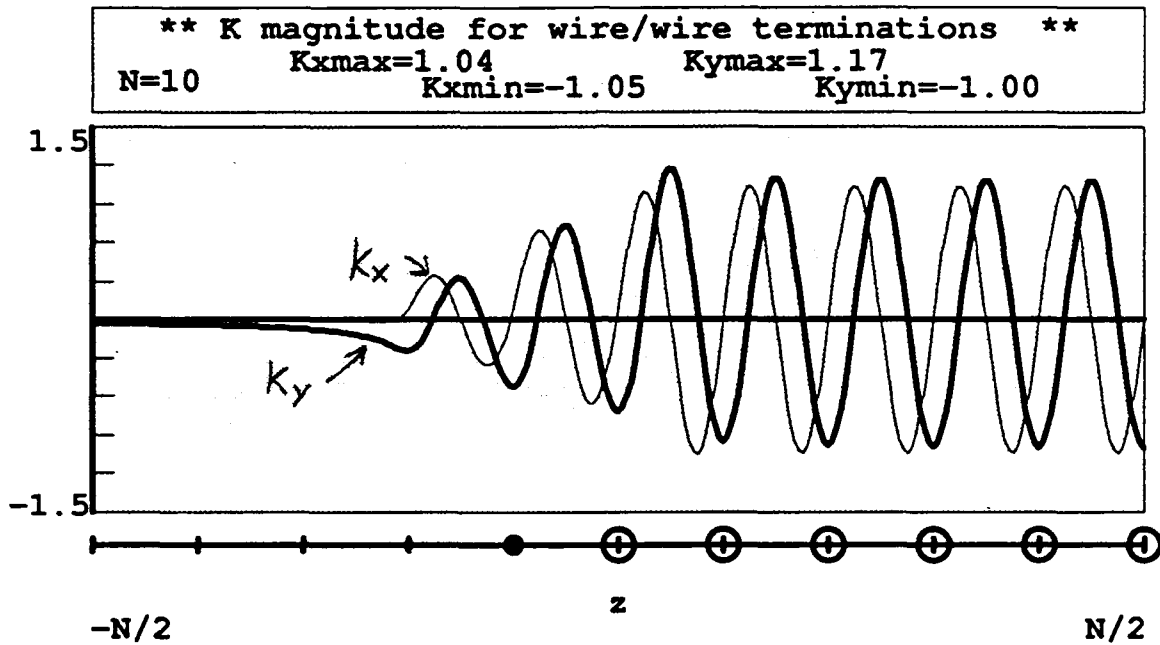
Figure 20 .

Combined plot of the K components along the z axis with 2 period taper.

The next step is to try loop termination to see if better results are achieved. If we apply a loop entrance and a wire exit (loop/wire) termination, we arrive at the values displayed in Figure 21. We see immediately that the range over which the y component is a single contributor is considerably shorter. The y component also starts with a positive value vice a negative one. This shortening and reversal is accompanied with a better symmetry seen throughout the displayed range as the maximum and minimum values show.

36

** K magnitude for loop/wire terminations **

N=10   Kxmax=1.02   Kymax=1.03
        Kxmin=-1.03   Kymin=-1.04
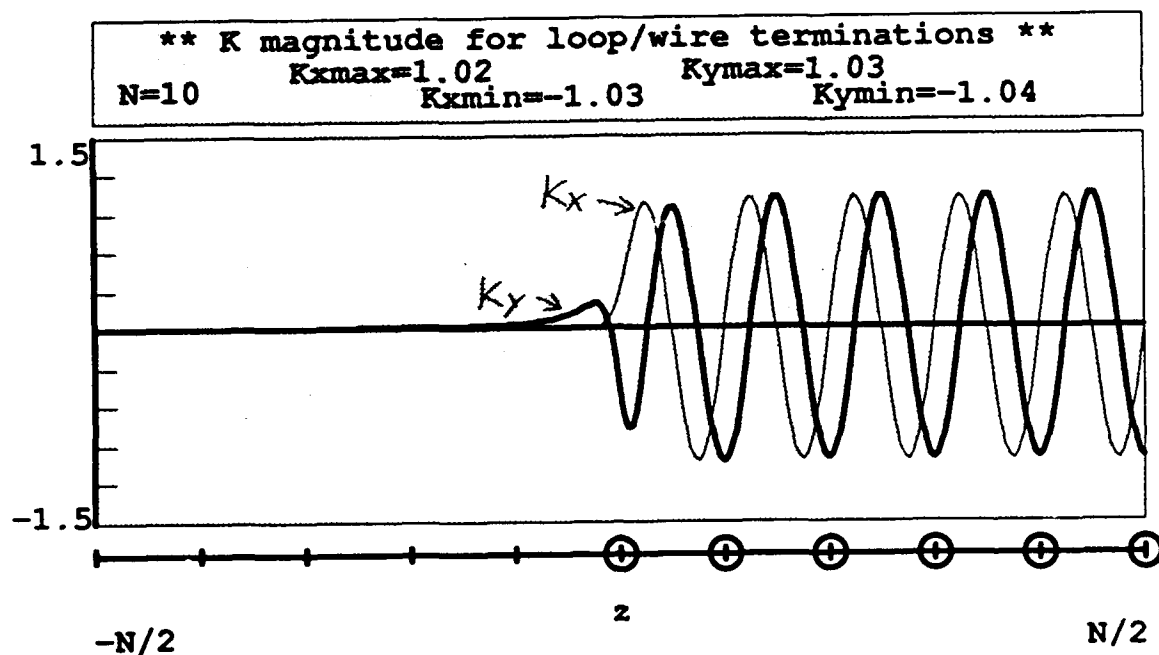
Figure 21 .

Combined plot of the K components along the z axis with no taper.

The improved symmetry should get better as we add tapering and it does. Figure 22 shows the combined components with a 2 period taper. The short range that the y component acts unopposed outside the entrance, and improved symmetry should prove to be a better design for the injection of electrons which will be explored later.
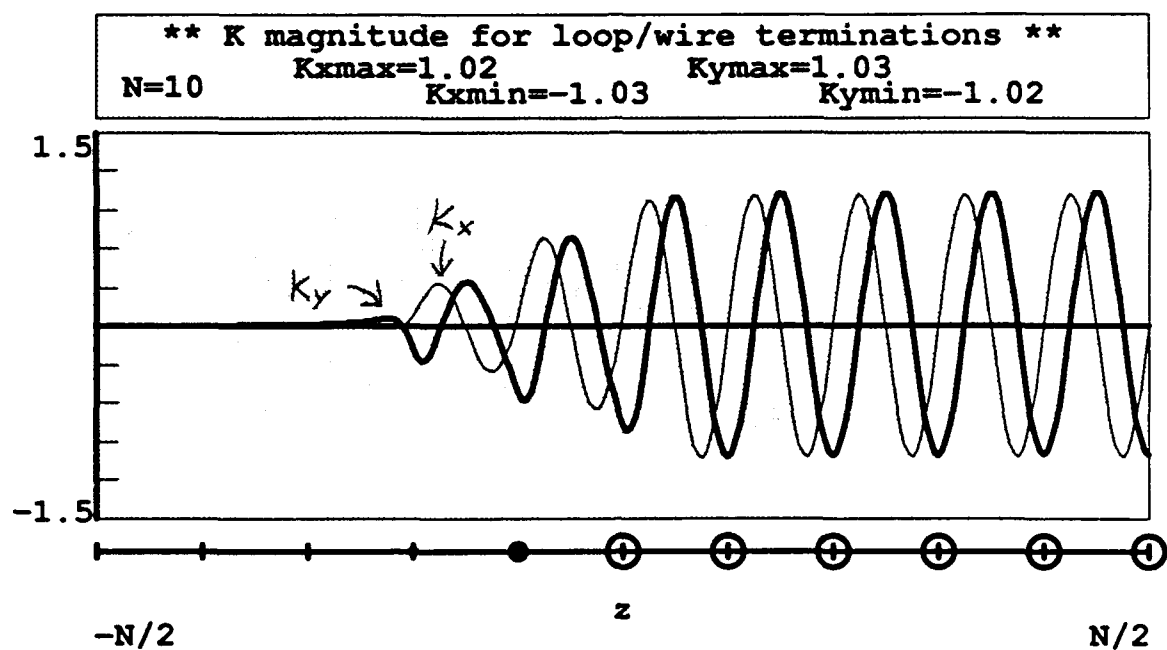
Figure 22 .

Combined plot of the K components along the z axis with 2 period taper.

The improved symmetry seen for the loop termination can be taken one step further by using it on the exit termination. This loop/loop termination would simulate an undulator with loop termination at both ends, and the power leads connected to the power supply via coaxial cable that give no magnetic field. We expect that this modification should have slightly better symmetry, since the dimensions of the compact FEL bring the exit termination close enough to have a noticeable effect on the entrance fields. If loop exit termination is added to the previous simulation, mixed results are achieved as shown in Figure 23. The range between minimum and maximum values for the components is reduced and the minimums and maximums are more constant than the previous case. Unfortunately, there is no clear cut indication that this termination technique

38

produces noticeable changes. Thus, we can only guess that this method would provide a better entrance field for incoming electrons. Since we have verified correlation to previous work [8], and established a guess as to which one should offer the most symmetrical magnetic fields, we need to find a better way of representing the fields. This section investigated the field amplitudes along the axis. The electrons will be following a helical trajectory through the undulator, and therefore, will experience fields off-axis in their travel through the undulator. Thus, modeling of off-axis fields needs to be explored.
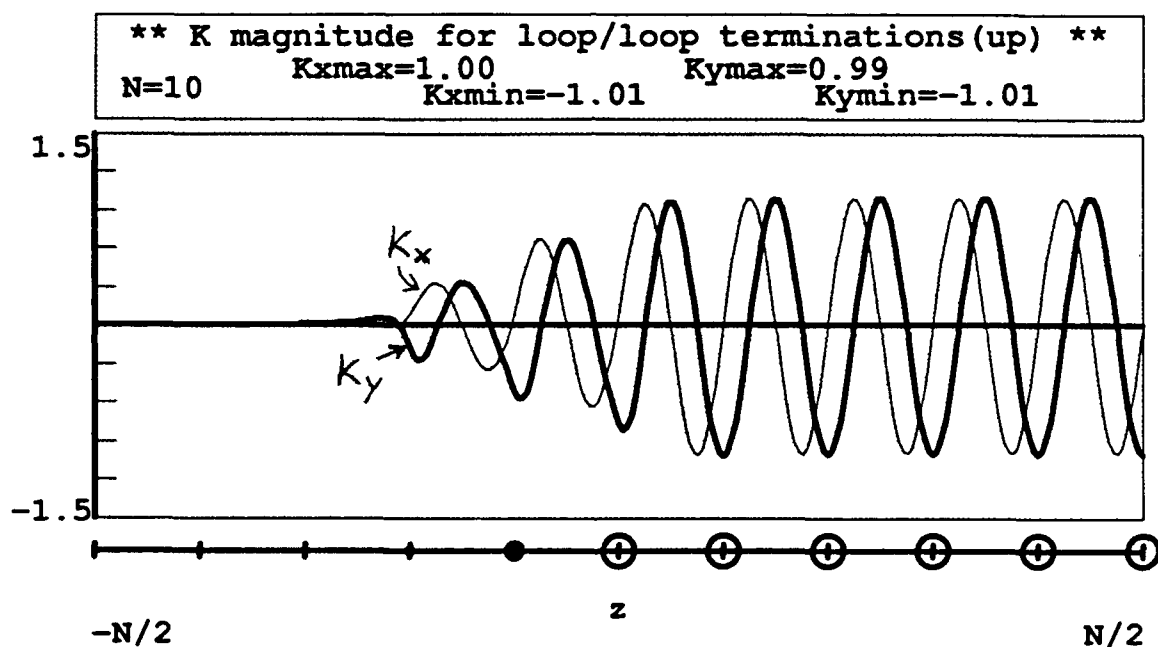

Figure 23 .

Combined plot of the K components along the z axis with 2 period taper.

b. Closeup of Entrance K Field

As mentioned previously, the fields off-axis are important to the calculation of the electron trajectories. A model can be envisioned that would contain the space vectors representing the magnetic field at any point in the undulator. This is the definition of a vector field, and while the subsequent electron beam trajectory calculations would be relatively simple, it is easy to see that any attempt to give accuracy to the vector field representation results in a computational nightmare. The sheer number of points needed for a three dimensional representation would overwhelm most computers. Thus, the model needs to be reduced in scope. The most obvious choice is to limit the boundaries of calculation inside the undulator which will reduce the number of points in the vector field that need to be calculated. Since the dimensions of the electron beam and the limits of off-axis motion are small, this is a reasonable simplification. The boundary could be as small as a fourth of the radius of the undulator and the number of points would then be reasonable for present-day computers to calculate and display. This method would be the best to pursue if a real beam of electrons is trying to be simulated. As mentioned in the background section, the density of the beam is on the order of 10^{12} electrons/cm^3. It is not practical to calculate the magnetic field for individual electrons when this many are involved. However, the model in this paper does not deal with a great number of electrons, only a small representative fraction. The calculations can be greatly speeded up by only calculating the magnetic field at the electron positions. This drastically reduces the number of calculations needed for accurate representation. The magnetic fields at the electron positions are used to calculate the force. This enables us to find the accelerations, and subsequent integrating finds the new positions.

Now that we have established that calculating a complete vector field is too hard, it would be even worse trying to represent it in some intelligible way. Therefore, we will pursue a planar representation of the vector field. The

integration technique was applied to the end of the undulator to see the stray field effect. The structure of the fields were illustrated by shade gradations corresponding to the value of the K vectors. The magnetic field values get very high close to the windings as one would expect. Therefore, to see the fine structure of the fields, positions only out to half the radius of the undulator are shown. The magnitude plot on the left has the windings on the outside of the undulator overlaid as dark black lines to help provide viewpoint recognition. To emphasize the need for tapering, simple wire termination is shown with positions from one period outside the undulator to one period inside the undulator as shown in Figures 24a and 24b. The white lines are contour lines of constant magnitude. Notice the skewed nature of the fields from the contour lines. As was conjectured previously, there are large asymmetrical fields at the entrance, and undesirable perturbations would distort the incoming electron trajectories.

*** K values vs. position ***

No taper λ_o=0.009m   g=0.2222

0.10 ▮▮▮▮▮ 1.73

-0.72 ▮▮▮▮▮ 0.72   :Kx

-0.75 ▮▮▮▮▮ 1.08   :Ky

|K| K_x K_y

z-λ_o

z

z+λ_o

-g/2   x   g/2 -g/2   x   g/2 -g/2   x   g/2

|K(0,0,0)| = 0.4691

Figure 24a .

Graphical representation of the K field composition in the x plane

from 1 period outside to 1 period inside the undulator.

The design is wire/wire termination.

*** K values vs. position ***

No taper $\lambda_O = 0.009m$ $g = 0.2222$

-0.88 ▮▮▮▮ 0.89 :Kx

0.10 ▮▮▮▮ 1.66 -0.59 ▮▮▮▮ 0.93 :Ky

$|K(0,0,0)| = 0.4691$

Figure 24b .

Graphical representation of the K field composition in the y plane

from 1 period outside to 1 period inside the undulator.

The design is wire/wire termination.

43

If we rerun the same scenario with a two period taper, we see by the contour lines and the maximum and minimum values that some of the asymmetrical nature has been reduced as shown in Figures 25a and 25b. Even though tapering has improved the picture, the overall symmetry of the wire termination scheme still leaves a lot to be desired. The next step is to apply loop termination to our model and see if our previous conclusion of better symmetry applies to off-axis fields.

Overall symmetry is seen when we apply loop/wire termination to our simulation as shown in Figures 26a and 26b. Even with no taper applied, the contour lines and the maximum and minimum values show a much more organized nature than before. This trend should get better if we apply tapering to our model, and it does in Figures 27a and 27b. The final simulation will be for loop/loop termination with no taper for comparison to the loop/wire termination (Figures 28a and 28b).

*** K values vs. position ***
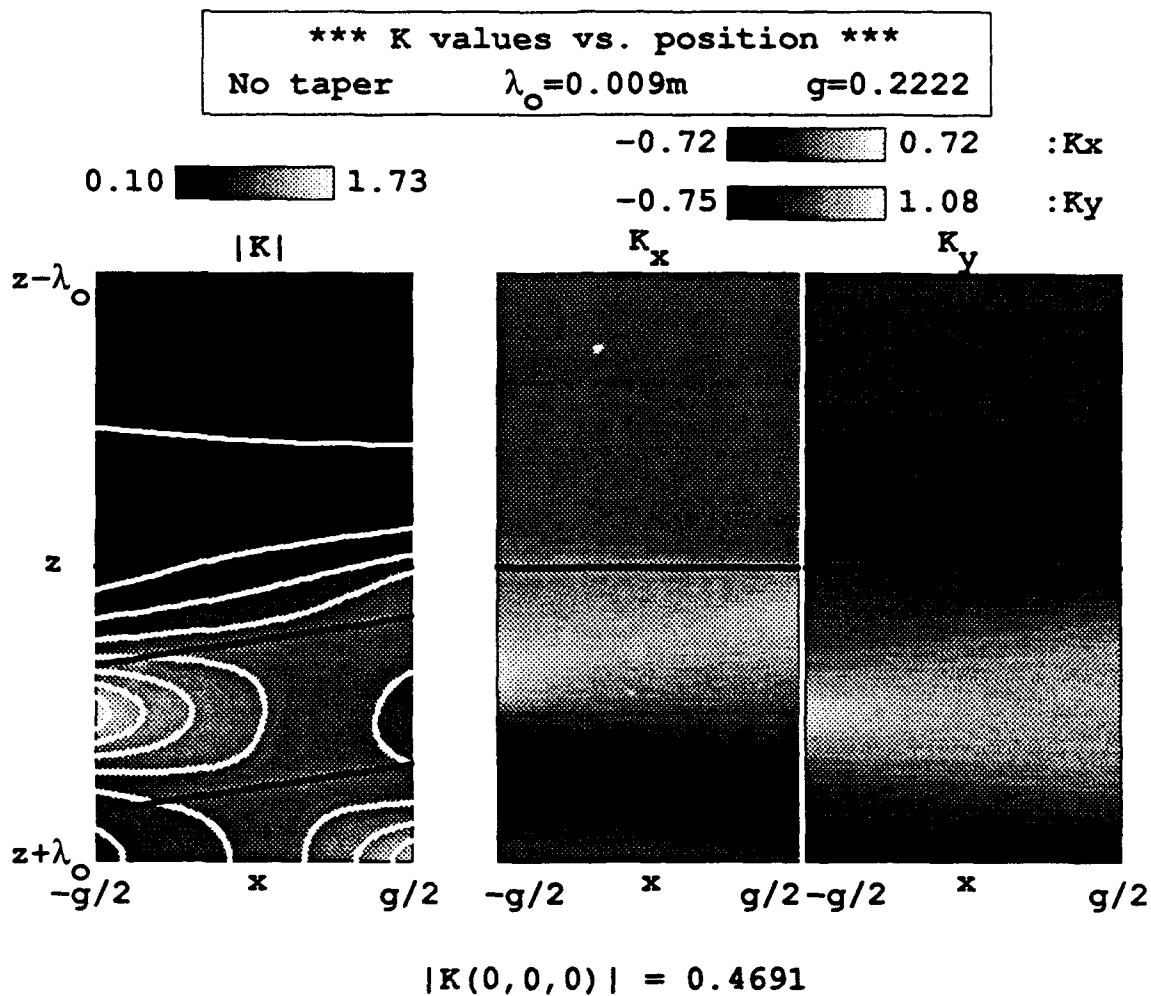
Tapered   λ_o=0.009m   g=0.2222

Figure 25a .

Graphical representation of the K field composition in the x plane

from 1 period outside to 1 period inside the undulator.

The design is wire/wire termination.

*** K values vs. position ***

Tapered $\lambda_o=0.009$m g=0.2222

-0.87 ▉▊▊▊ 0.87 :Kx

0.40 ▉▊▊▊ 1.64

-0.63 ▉▊▊▊ 0.83 :Ky

|K| K_x K_y

$z-\lambda_o$

z

$z+\lambda_o$

$-g/2$ y $g/2$ $-g/2$ y $g/2$ $-g/2$ y $g/2$
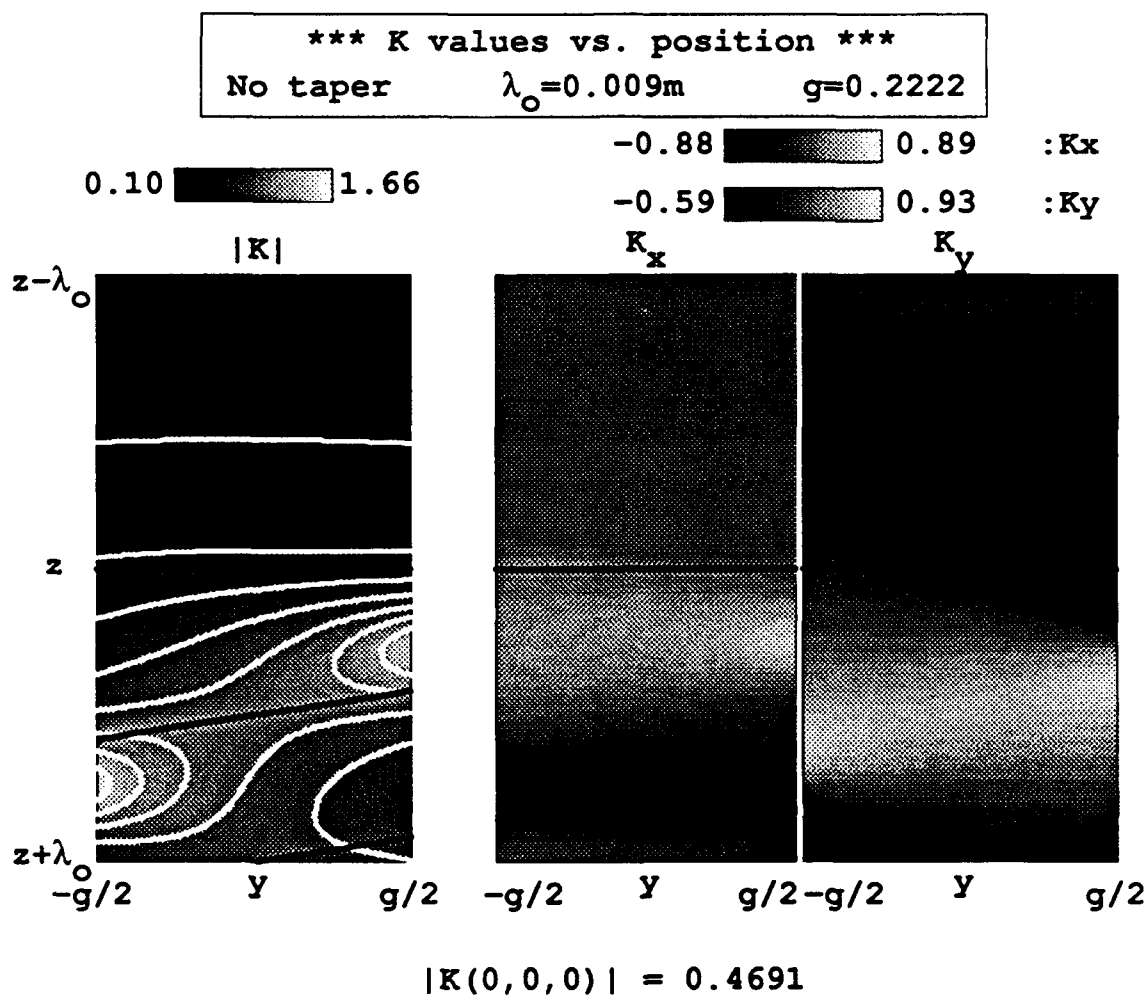
|K(0,0,0)| = 0.7414

Two period taper

Figure 25b .

Graphical representation of the K field composition in the y plane

from 1 period outside to 1 period inside the undulator.

The design is wire/wire termination.

*** K values vs. position ***
No taper $\lambda_o = 0.009$m   g=0.2222

−1.08 ▮▮▮ 1.03   :Kx

0.03 ▮▮▮ 1.53

−1.26 ▮▮▮ 1.17   :Ky

$|K|$ K_x K_y

$z-\lambda_o$

z

$z+\lambda_o$

−g/2   x   g/2   −g/2   x   g/2   −g/2   x   g/2

$|K(0,0,0)| = 0.5505$

Figure 26a .

Graphical representation of the K field composition in the x plane

from 1 period outside to 1 period inside the undulator.

The design is loop/wire termination.

Figure 26b .

Graphical representation of the K field composition in the y plane

from 1 period outside to 1 period inside the undulator.

The design is loop/wire termination.

*** K values vs. position ***
Tapered $\lambda_o = 0.009$m $g = 0.2222$

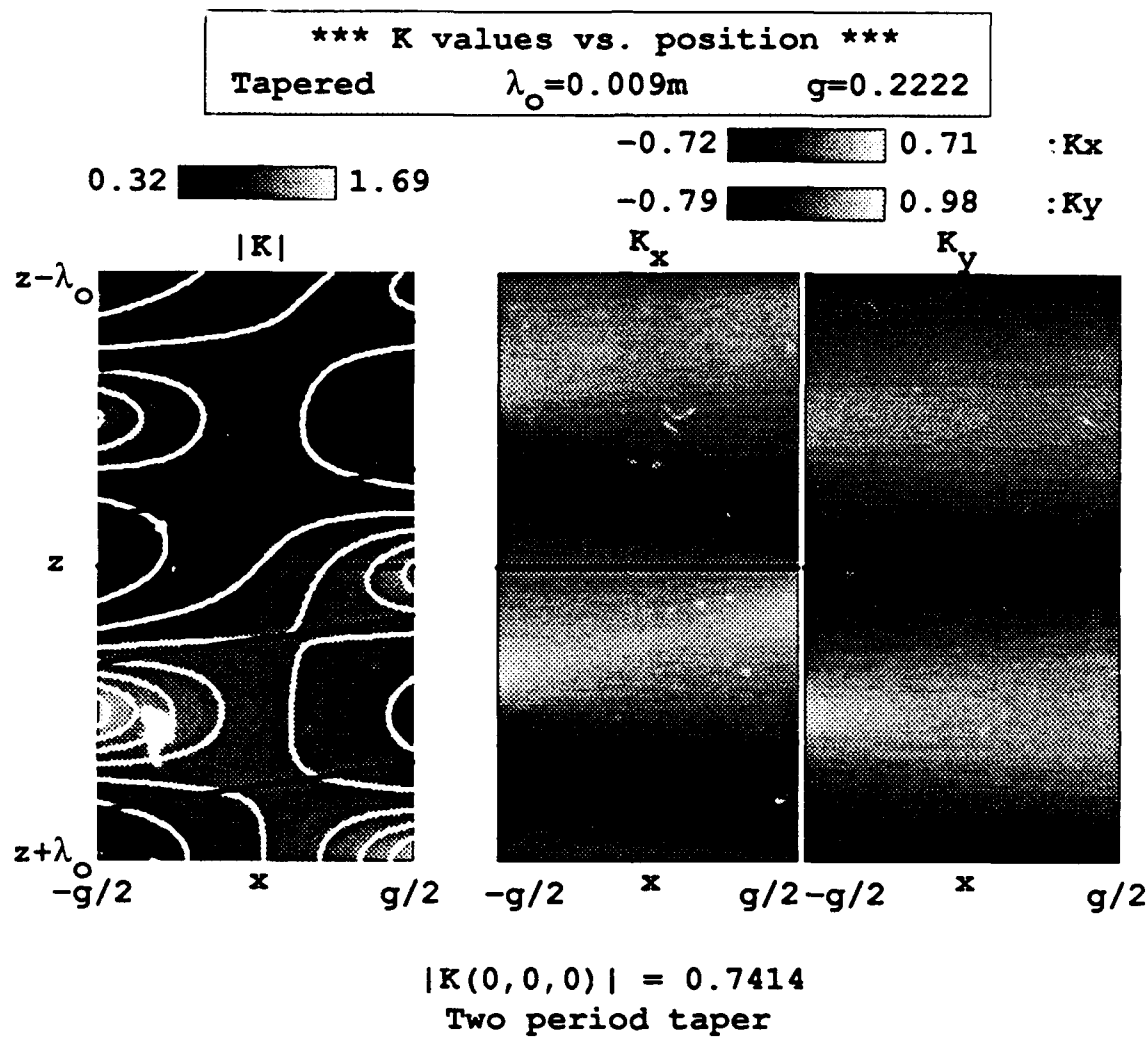$|K(0,0,0)| = 0.8508$
Two period taper

Figure 27a .

Graphical representation of the K field composition in the x plane

from 1 period outside to 1 period inside the undulator.

The design is loop/wire termination.

49

*** K values vs. position ***

Tapered $\lambda_o = 0.009$m   g=0.2222

−1.25 █████ 1.23   :Kx

0.50 █████ 1.52   −1.10 █████ 1.05   :Ky

|K| K_x K_y

$z-\lambda_o$

z

$z+\lambda_o$

−g/2   y   g/2   −g/2   y   g/2   −g/2   y   g/2
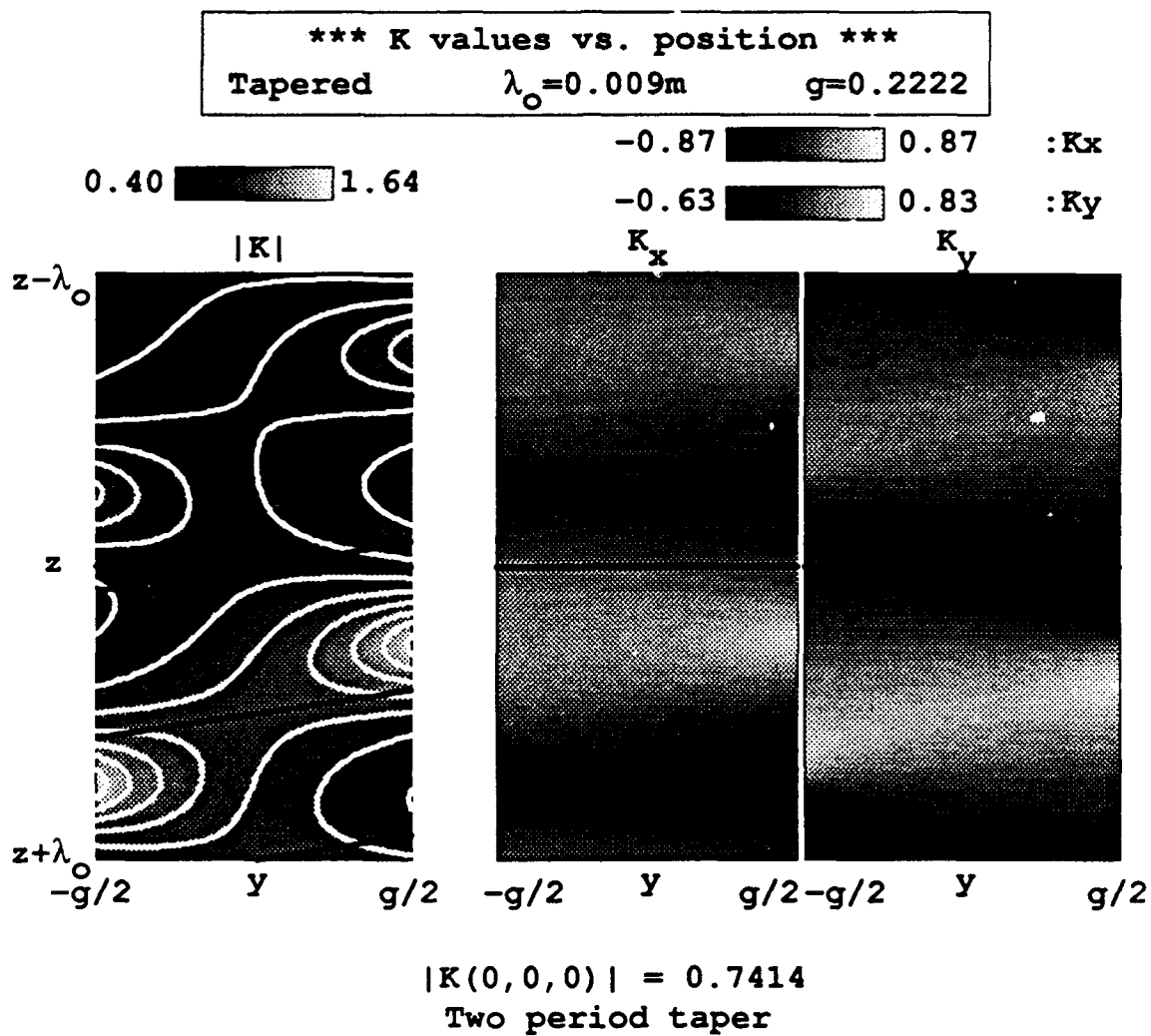
|K(0,0,0)| = 0.8508

Two period taper

Figure 27b .

Graphical representation of the K field composition in the y plane

from 1 period outside to 1 period inside the undulator.
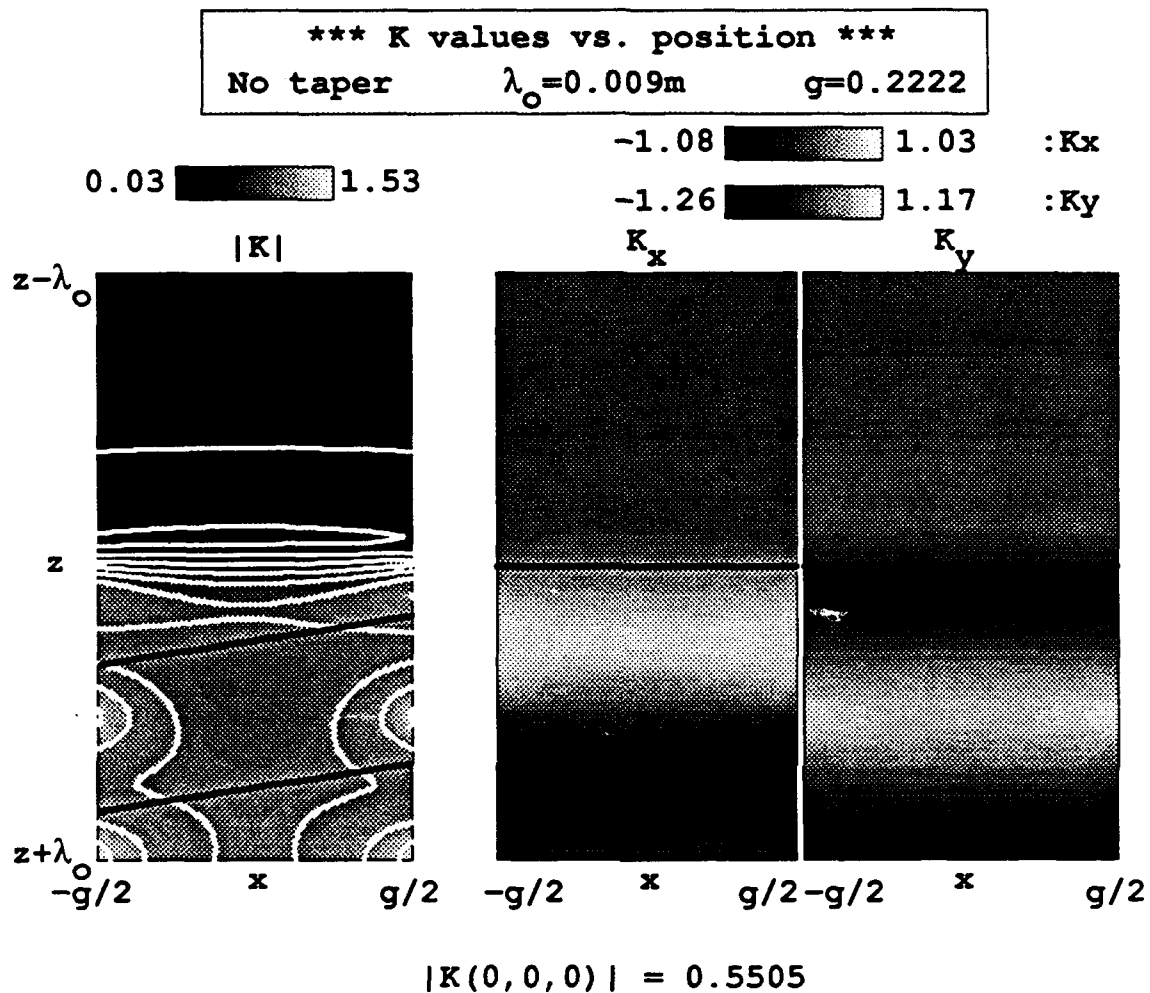
The design is loop/wire termination.

Figure 28a .

Graphical representation of the K field composition in the x plane

from 1 period outside to 1 period inside the undulator.

The design is loop/loop termination.

*** K values vs. position ***

No taper λ_o=0.009m   g=0.2222

0.03 ▮▮▮ 1.49 |K|

-1.23 ▮▮▮ 1.19   :Kx
-1.23 ▮▮▮ 0.97   :Ky

K_x K_y

z-λ_o

z

z+λ_o

-g/2   y   g/2   -g/2   y   g/2-g/2   y   g/2
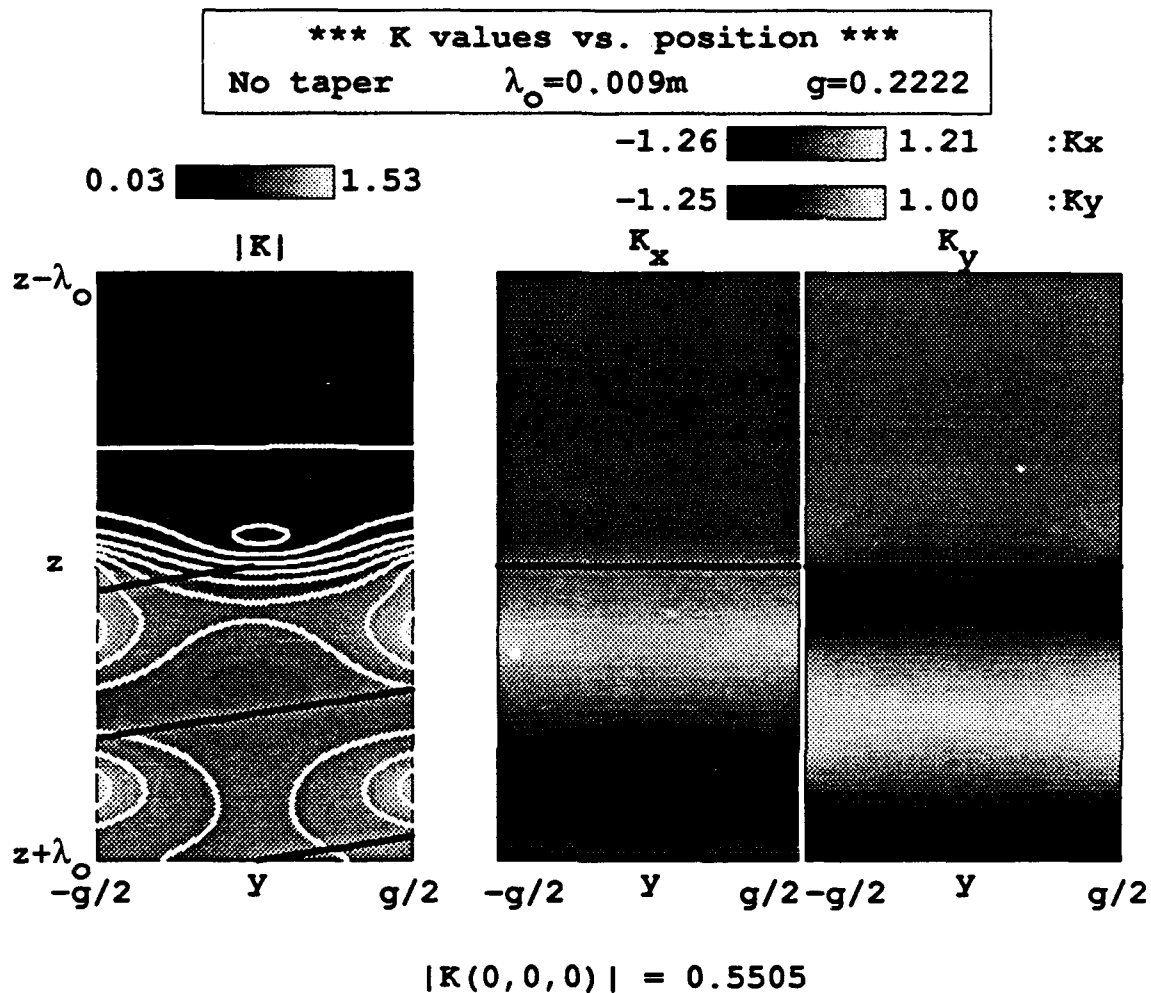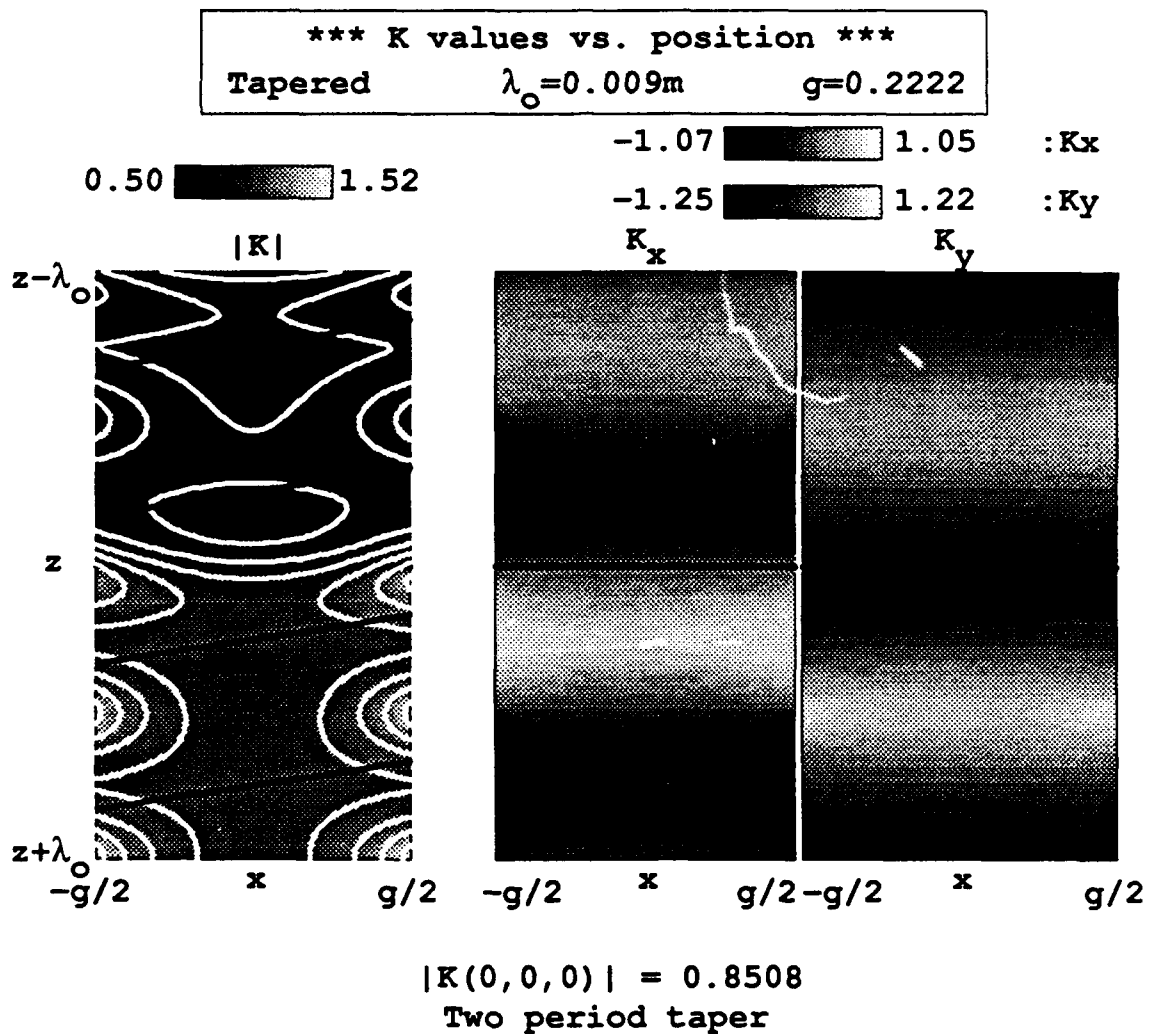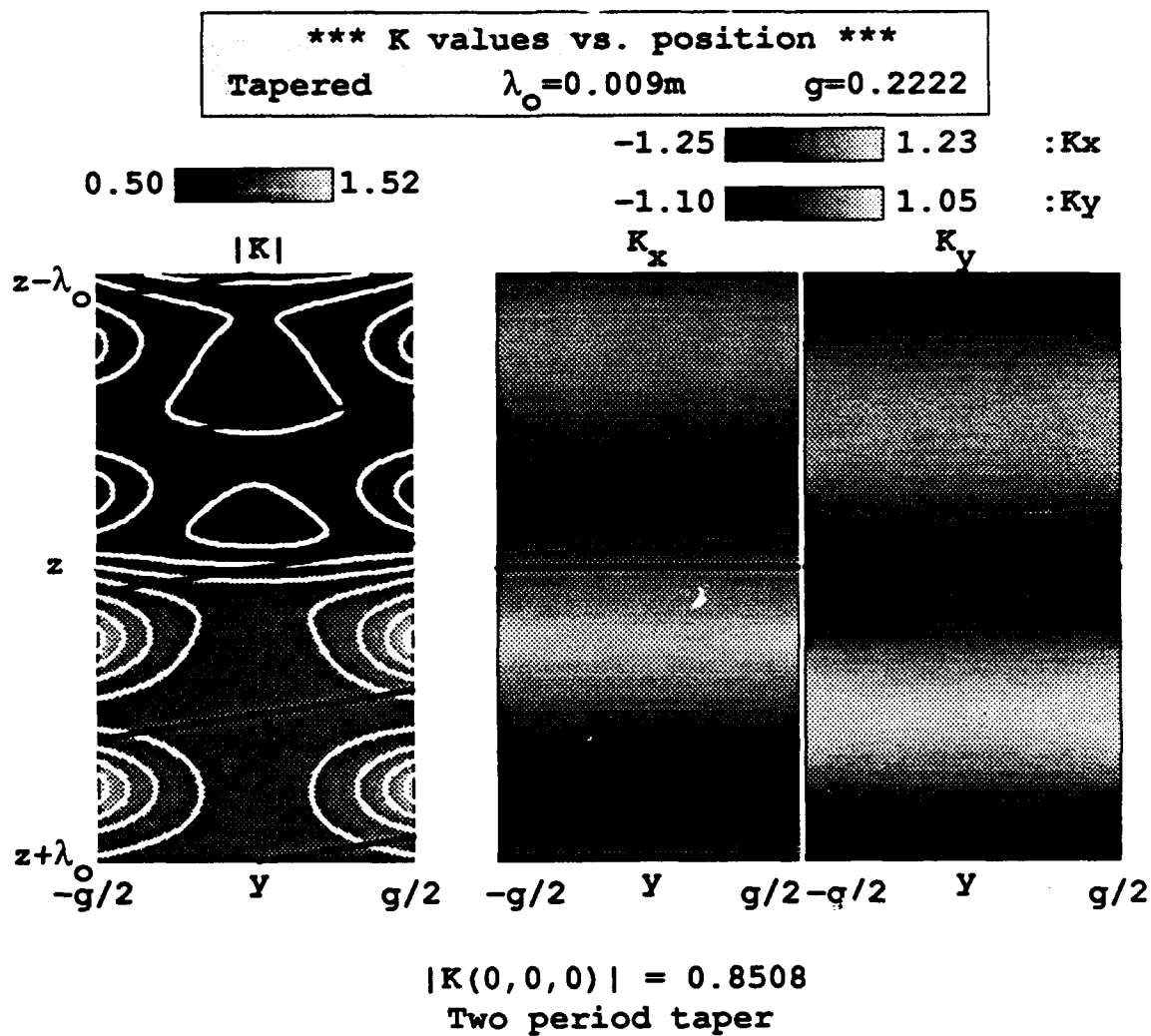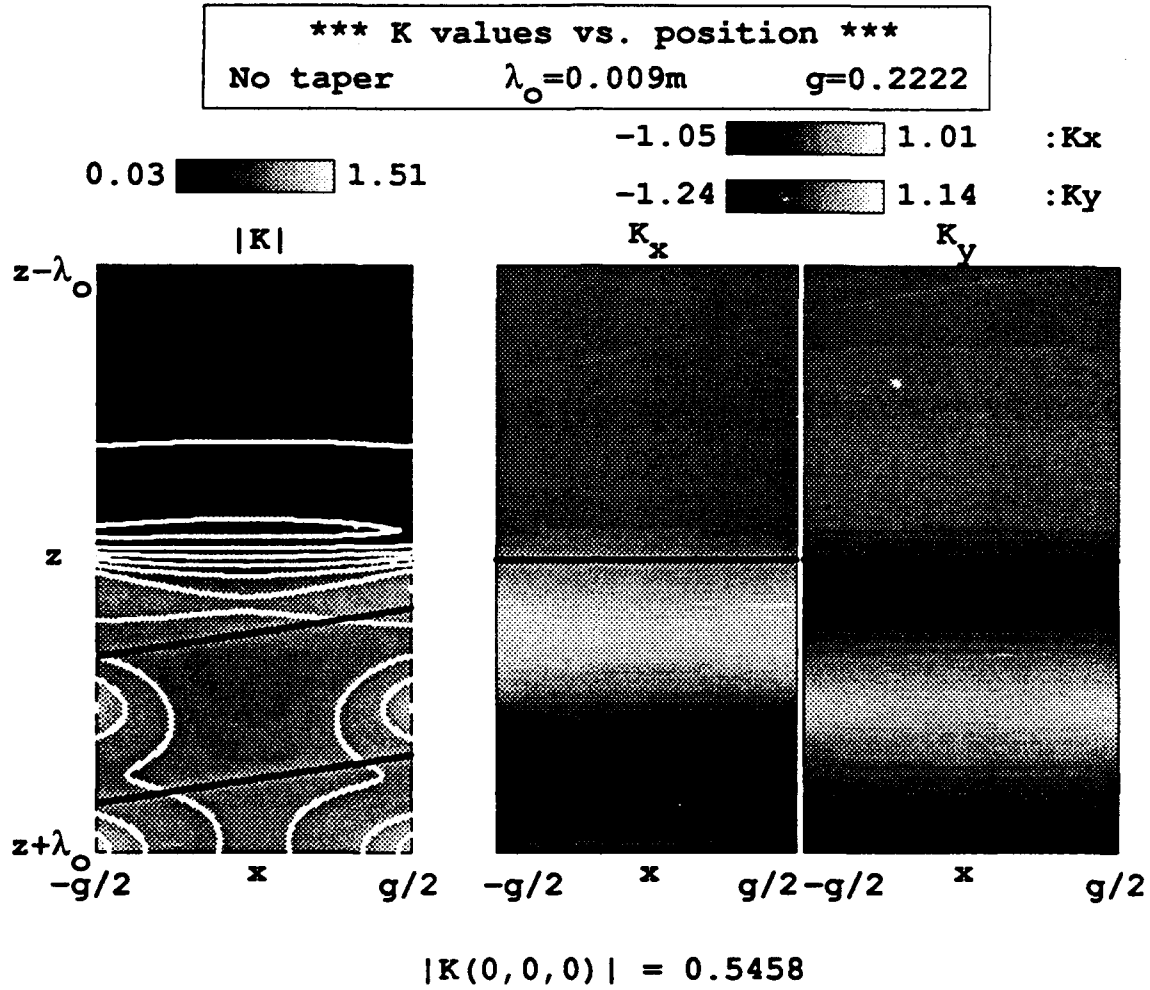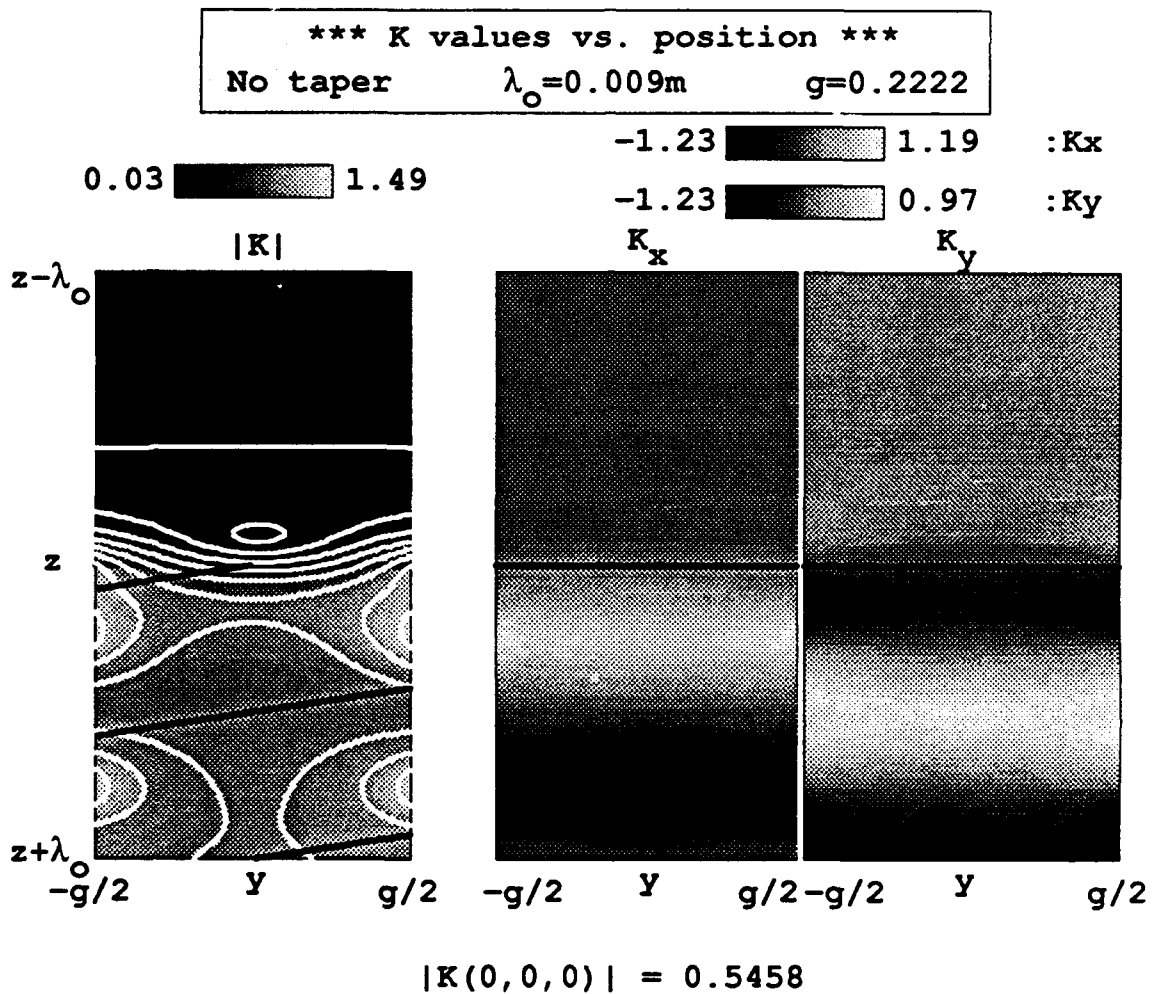
|K(0,0,0)| = 0.5458

Figure 28b .

Graphical representation of the K field composition in the y plane

from 1 period outside to 1 period inside the undulator.

The design is loop/loop termination.

Unfortunately, the exit termination representation does not give a clear improvement of the stray field structure. The resolution of optimum design will have to wait for a different representation of the fields. To pursue this avenue, there is a possibility that the view shown is too narrow. Thus, we shall expand the displayed K field to show an enlarged view.

c. K Field Over Five Periods Inside and Out

We next apply the terminations to a display that shows positions along the z axis from 5 periods outside the undulator to the middle of our undulator. Again, shade gradations show the detailed structure of the stray fields at work on the entrance to the undulator as shown in Figure 29. The structure seen is quite complicated and several trends are evident. The first is the contour lines along the axis of the undulator. The contour lines show that the fields are not uniform along the axis where they should be the most symmetrical. Also, the light area right at the entrance to the undulator indicates the strongest magnetic field is present right at the entrance. This abrupt field change may prove detrimental to the electron trajectories investigated shortly. If the contour lines close to the coil positions are studied, the x plane reveals an interesting feature. The contour lines have a magnitude sinusoidal with the z direction. The magnitude of the contours gets increasingly symmetrical as the undulator is traversed indicating the termination wires affect the magnetic field structure all the way to the center of the undulator. This effect is not evident in the y plane. We could conclude that electron trajectories would be significantly affected by this type of design, especially in the x plane. Since the stray field structure looked more symmetrical for loop termination, we should see if this applies to our expanded view of the undulator fields.

Figure 29 .

Graphical representation of the K field composition in the x and y plane
for wire/wire termination. The displayed positions are from 5 periods
outside the undulator to 5 periods inside the undulator.

If loop/wire termination is applied to our model undulator, we can
see major changes in the representation of the fields as shown in Figure 30. The
overall symmetry of the structure is better, especially in the x plane. The

sinusoidal variance of the fields close to the windings now appears to be reversed, but at a significantly lower amplitude. The abrupt change in field intensity at the entrance is also reduced in intensity. The close spacing of the contour lines at the entrance signify a significant field gradient right at the entrance that seems to extend for a much shorter distance than wire/wire termination. An interesting feature is the significant asymmetry at about 1 undulator period inside the undulator. This is evident in both the x and y plane. The conclusion taken from this representation is that this design provides better magnetic field symmetry and should have a less detrimental effect on the incoming electron trajectories. The final design considered is for loop/loop termination as shown in Figure 31.

** K values entering undulator **

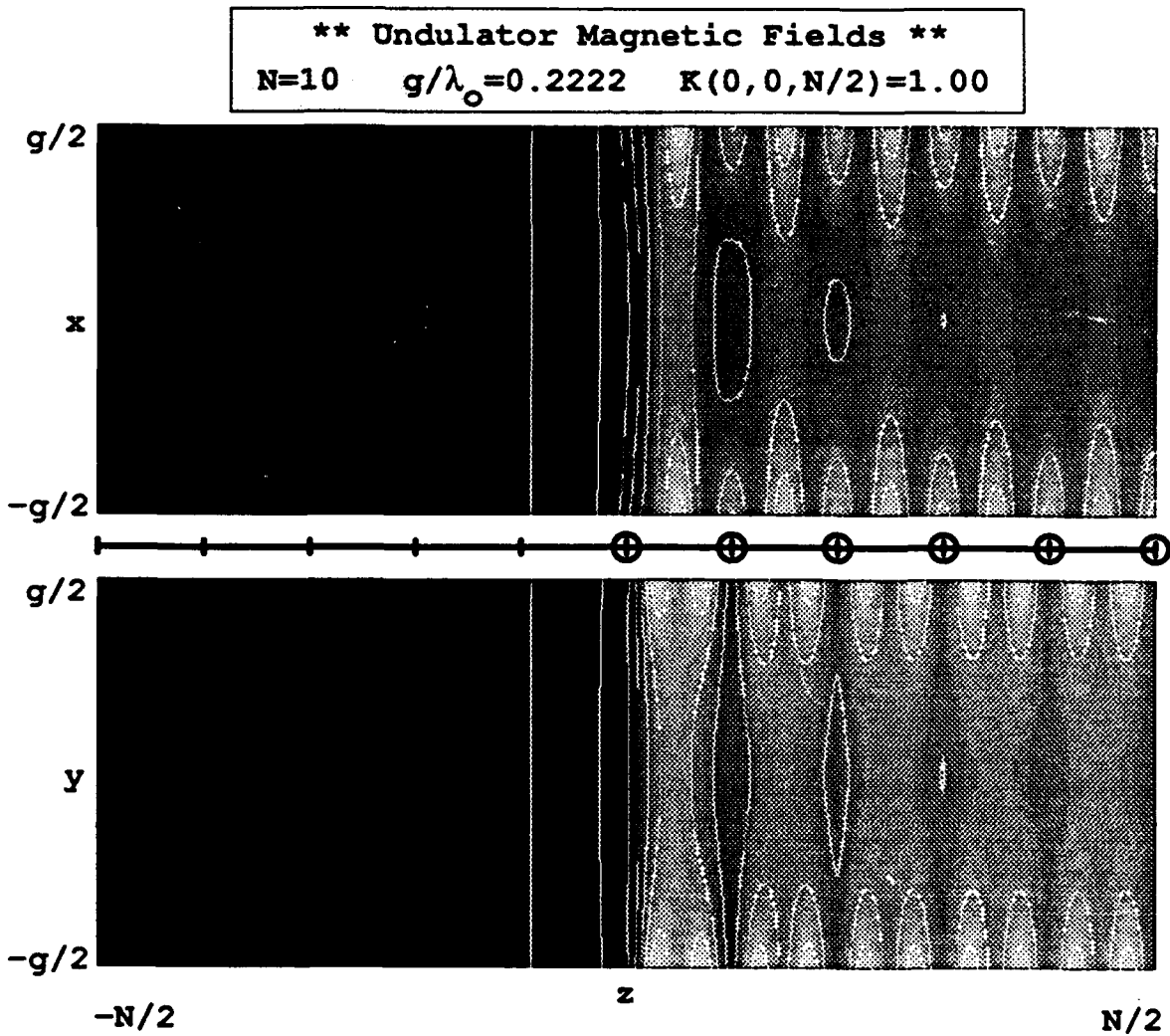N=10   g/λ_o=0.2222   K(0,0,N/2)=1.00

Figure 30 .

Graphical representation of the K field composition in the x and y plane

for loop/wire termination. The displayed positions are from 5 periods

outside the undulator to 5 periods inside the undulator.

Looking at the plot, we still see the ambiguity we had before with

this design. Since the construction of the undulator is close to loop/wire

configuration, it is not surprising that we see the basic symmetry throughout the

56

displayed fields. The major difference seen is a sharp reduction in the sinusoidal variations of the contour lines close to the windings. The increased symmetry seen should prove to be the best design of the termination schemes explored.
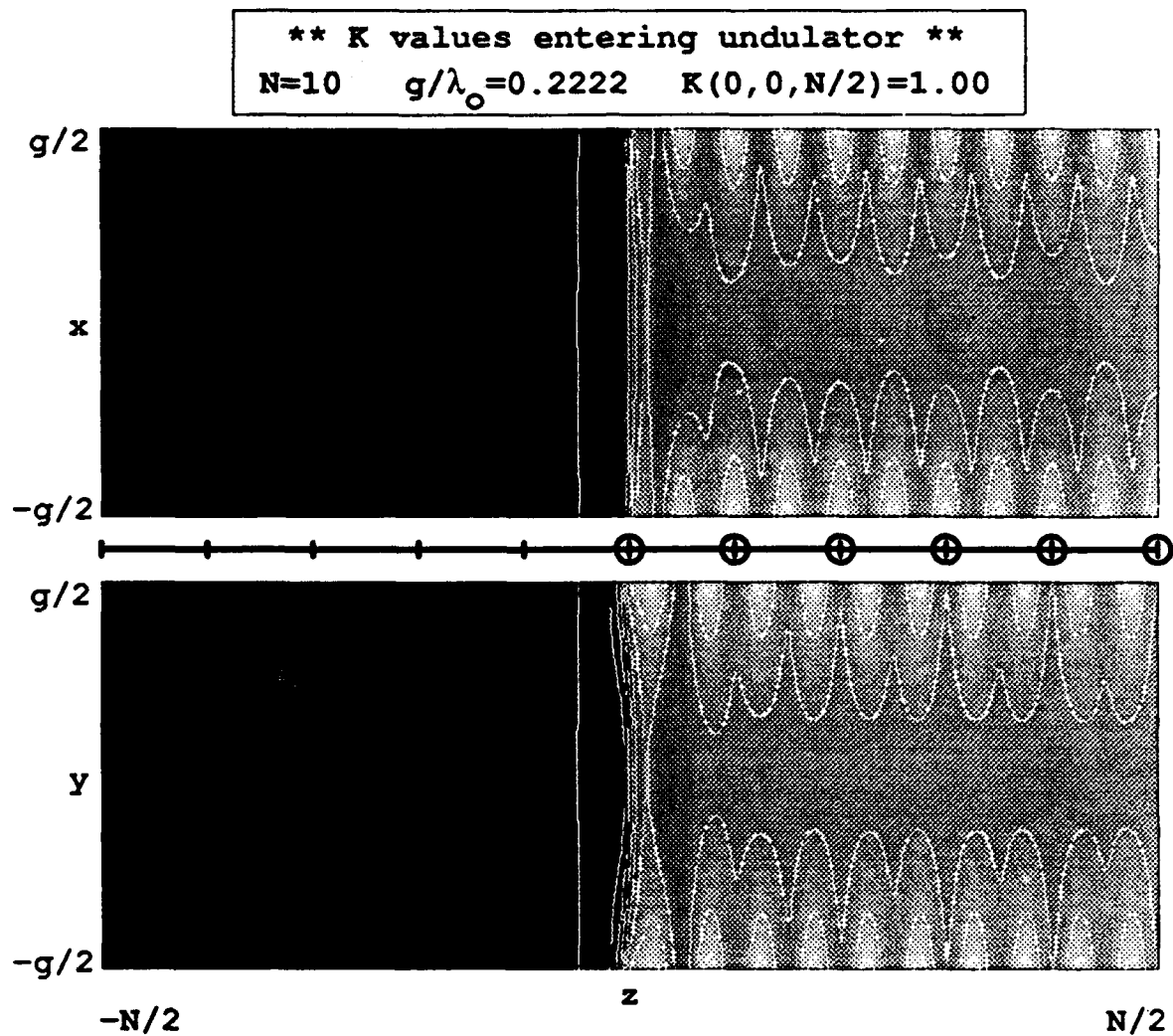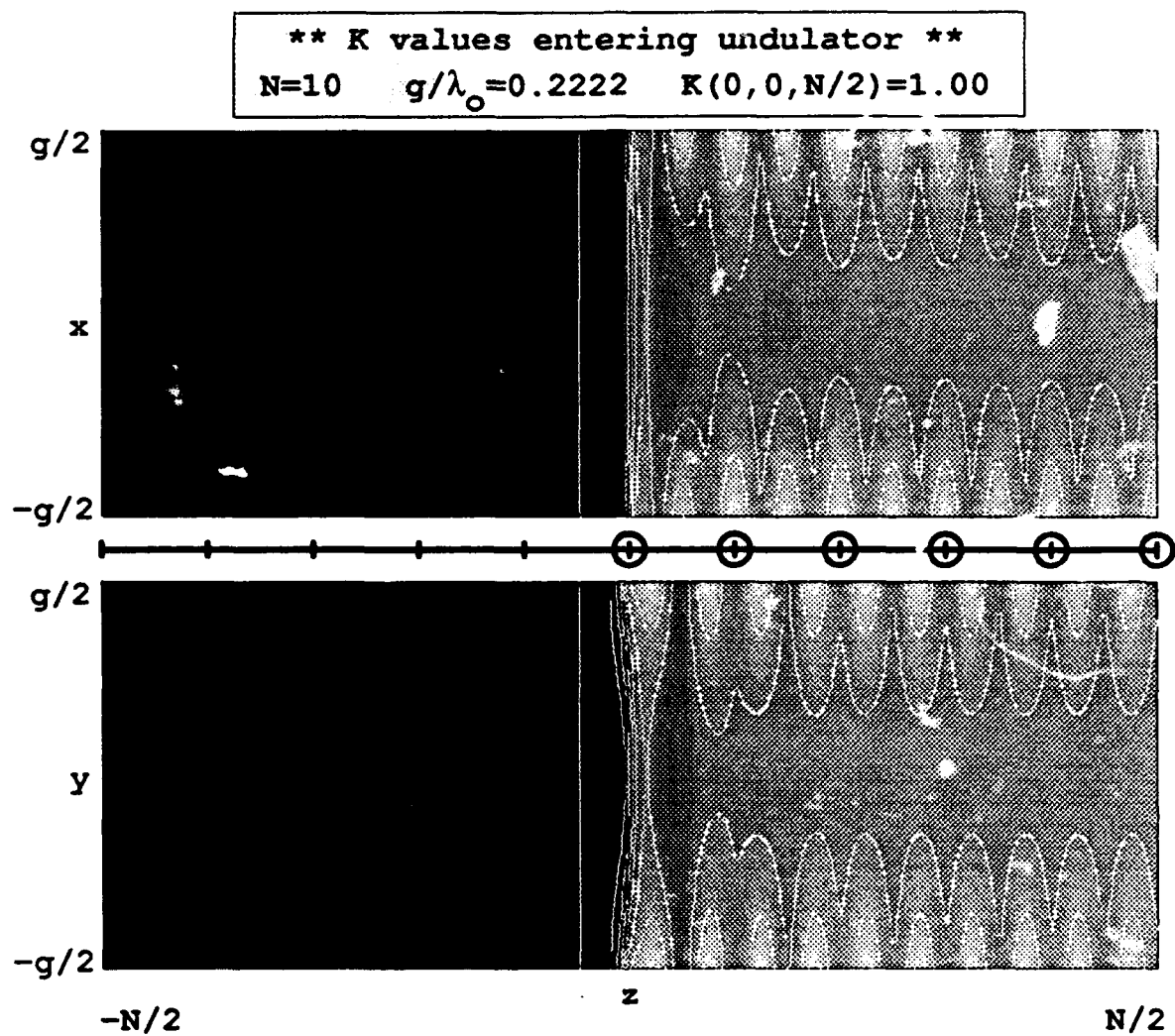
Figure 31 .

Graphical representation of the K field composition in the x and y plane
for loop/loop termination. The displayed positions are from 5 periods
outside the undulator to 5 periods inside the undulator.

B. REPRESENTATION OF TRAJECTORIES

1. Theory

As mentioned previously, the magnetic field is found at the electron position only when calculating the electron motion. Using the magnetic field, the force is found using the Lorentz Force equation (5). We neglect the presence of light ($\vec{E}_r = \vec{B}_r = 0$), and use the calculated magnetic field to integrate the motion. We know that

$$\frac{d}{dt}(\gamma\vec{\beta}) = -\frac{e}{m}[\vec{\beta} \times \vec{B}] \quad \text{and if} \quad \dot{\gamma} = 0 \tag{6}$$

$$\Rightarrow \quad \dot{\vec{\beta}}_\perp = -\frac{e}{\gamma m}[\beta_y B_z - \beta_z B_y , \beta_z B_x - \beta_x B_z , 0] \quad,$$

$$\dot{\beta}_z = -\frac{e}{\gamma m}[\beta_x B_y - \beta_y B_x] \quad. \tag{32}$$

Recall from (17) that

$$\beta_\perp \simeq \frac{K}{\gamma} \ll 1 \quad, \tag{33}$$

so that $\dot{\beta}_z \simeq 0$. Then, using $\beta_z \simeq 1$, we have the approximate z motion, $z = z_o + \tau L$ where $\tau = ct/L$. Using $\beta_{x,y} \ll \beta_z$, we also find that

$$\dot{\vec{\beta}}_\perp \simeq \frac{e}{\gamma m}[B_y , -B_x] \quad, \tag{34}$$

which leads us to

$$\frac{\ddot{x}}{c} \simeq \frac{e}{\gamma m}B_y \quad, \quad \frac{\ddot{y}}{c} \simeq -\frac{e}{\gamma m}B_x \quad. \tag{35}$$

Using $dt = Ld\tau/c$, we find that

$$\overset{\circ\circ}{x} = \frac{L^2 e B_y}{\gamma mc} \quad \text{and} \quad \overset{\circ\circ}{y} = -\frac{L^2 e B_x}{\gamma mc} \quad, \tag{36}$$

where $(\overset{\circ}{}) = d(\ )/d\tau$. Finally, with $x/\lambda_o \to x$, $y/\lambda_o \to y$, and $z/\lambda_o \to z$, we

simplify these expressions to

$$\overset{\circ\circ}{x} \; = \; \frac{2\pi N^2 K_y}{\gamma} \qquad , \qquad \overset{\circ\circ}{y} \; = \; -\frac{2\pi N^2 K_x}{\gamma} \qquad , \qquad z \; = \; z_o + N\tau \quad , \quad (37)$$

where

$$K_{x,y} \; = \; \frac{eB_{x,y}\lambda_o}{2\pi mc} \quad .$$

The Euler-Cromer integration method will be used to update the electron position as it travels through the fields represented in our simulated undulator [10].

2. Example of Ideal Injection

The previous discussion explores the technique used to determine the electron trajectories. This section describes ideal injection where the electron is moving tangent to the motion it would describe if it were inside of an infinite undulator. In our case, this motion is a helix centered on the z axis. Good injection is desirable in experiments because it establishes a smooth transition into the undulator and increases the gain of the FEL.

The exact trajectories in a helical undulator are

$$\vec{\beta} \; = \; \left[-\frac{K}{\gamma}\cos(\omega_o t) \; , \; -\frac{K}{\gamma}\sin(\omega_o t) \; , \; \beta_o \right] \quad , \qquad (38)$$

where

$$\omega_o \; = \; \beta_o k_o c \; = \; \frac{\beta_o 2\pi c}{\lambda_o} \quad \text{and} \quad \beta_o^2 \; = \; 1 - \frac{1 + K^2}{\gamma^2} \quad .$$

By integrating, we can get the exact equation for the electron position at any time t,

$$\vec{x} \; = \; \left[-\frac{K\lambda_o}{2\pi\gamma\beta_o}\sin(\omega_o t) \; , \; \frac{K\lambda_o}{2\pi\gamma\beta_o}\cos(\omega_o t) \; , \; \beta_o ct \right] \quad . \qquad (39)$$

At time t = 0, the trajectory describes the maximum angle with the z axis in the x-

60

z plane. Therefore, to describe the angle that is tangent to the helix, we define the angle θ, where it can be shown that,

$$\theta_x = \frac{dx}{dz} = \beta_x(0) = -\frac{K}{\gamma} \quad , \quad \theta_y = 0 \quad \text{if } \beta_z(0) = \beta_o \simeq 1 \quad ,$$

and

$$\Delta x = 0 \quad , \quad \Delta y = \frac{K\lambda_o}{2\pi\gamma\beta_o} \quad . \tag{40}$$

By substituting the parameters of our model undulator with $K = 1$, $\gamma = 30.35$ and $\lambda_o = 0.9$cm. into (40), we find that the perfect injection angle is $\theta_x \simeq 0.033$ radians, and $\Delta y = 0.0053$ (non-dimensional units).

3. Results

Now that we have developed the theory of electron trajectory calculation, we need to develop some way of displaying the resulting information. To add some continuity, the electron trajectories will be calculated and overlaid on the same K field shown previously in Figures 41, 43, and 45. Although simple in principle, there are a couple of complicating features that need to be addressed. The first is the electrons' initial position and angle inside the beam. The second is finding some way of estimating the injection parameters so that optimization of undulator designs can be discerned. The easiest way to accomplish this is to determine a "characteristic" angle and position offset that the stray magnetic fields will bend the individual electrons through.

The individual electrons inside the simulated electron beam are given an initial position and angle consistent with a characteristic beam quality factor called "emittance". The definition for emittance is $\varepsilon_x = 2\pi \bar{x} \bar{\theta}_x$ and $\varepsilon_y = 2\pi \bar{y} \bar{\theta}_y$, and it is assumed in this paper that $\varepsilon_x = \varepsilon_y$. The quantity $\bar{x}$ is the rms initial position spread of electrons along the x direction and $\bar{\theta}_x$ is the rms initial angular spread of electrons from the axis of the undulator along the x direction. Either the

rms position spread, $\bar{x}$, or the rms angular spread, $\bar{\theta}_x$, can be changed by external focusing fields prior to entrance into the undulator, but their product, ε_x, is fixed. Thus, arbitrary values for $\bar{x}$ and $\bar{\theta}_x$ are chosen such that $\bar{x} = 2r_e$, where r_e is the electron beam radius, and $\bar{\theta}_x = 4r_e/N$. The value used in this paper is $r_e = 0.1g$ where $g = 2\text{mm}$.

The electrons are initially started at 5 undulator periods away from the beginning of the first taper. The electrons are injected at a position and angle such that the resulting trajectories execute helical motion centered around the z axis. Since there are a large number of designs, we need to find some method of determining the optimum tapering scheme for each termination. The initial angles and positions are estimated by a calculated characteristic deflection angle and position offset for each design. By finding the minimum characteristic deflection angles and position offsets, the optimum taper for each end termination is determined. Using (37), we have

$$\overset{oo}{x} = \frac{2\pi N^2 K_y}{\gamma} = \frac{dv_x}{d\tau} \qquad \text{and} \qquad \overset{oo}{y} = -\frac{2\pi N^2 K_x}{\gamma} = \frac{dv_y}{d\tau} \quad .$$

With $d\tau = dz/N$, it can be shown that on the undulator axis,

$$dv_x = \frac{2\pi N}{\gamma} \int_{-(5+t)}^{5} K_y(0,0,z)\,dz \quad ,$$

where t is the number of tapered periods. The initial transverse velocity gives the initial transverse angle, so that

$$dv_x = \frac{dx}{d\tau} = \frac{dxN}{dz} = \theta_x N \quad . \tag{41}$$

Therefore, the characteristic angle of an electron traveling into the undulator is

$$\theta_x = \frac{2\pi}{\gamma} \int_{-(5+t)}^{5} K_y(0,0,z)\,dz \qquad \text{and} \qquad \theta_y = -\frac{2\pi}{\gamma} \int_{-(5+t)}^{5} K_x(0,0,z)\,dz \quad . \tag{42}$$

To find the characteristic position offset, we continue the previous derivation and apply (41) to (42), and integrate dx over the length of the trajectory. The resulting

offset is given by

$$\Delta x = \frac{2\pi}{\gamma} \int_{(5+t)}^{5} dz' \int_{(5+t)}^{z'} K_y(0,0,z)\, dz \quad \text{and}$$

$$\Delta y = -\frac{2\pi}{\gamma} \int_{(5+t)}^{5} dz' \int_{(5+t)}^{z'} K_x(0,0,z)\, dz \quad . \tag{43}$$

By translating (42) and (43) into a computer program, the different terminations and tapers can be evaluated in tabular form shown in Tables 1 to 3. The type of tapering explored was either linear or a smooth curve fit to the successive current reductions. If more than a three period taper is used, there is a possibility of designing the taper such that the stepwise current reductions do not follow a straight ramping function. The current reductions can be tailored to follow a curved function. The curve fit was tried with both a tangent function and a smooth curve (determined by hand) representing the current reductions.

It is important to note several points about the characteristic angles and positions determined. The first is that the K values are confined along the z axis. Since the actual electron trajectories do not exactly follow the z axis, the deflection angles and position offsets found will not exactly match the offsets required for injection. However, the trends found in the tables are a good indicator of optimum tapering schemes for each termination design. The second point is the integration length of the y component. Referring back to Figures 18 to 23, notice the difference between the component K values along the z axis. The K_x component ends on an even period at z = 5. This is not true for the K_y component. The integration distance for the y component is taken to be one-quarter period less to account for the alternating values seen by the incoming electron. Therefore, the modified characteristic angle becomes

$$\theta_x = \frac{2\pi}{\gamma} \int_{(5+t)}^{5} K_y(0,0,z)\, dz \quad \text{and} \quad \theta_y = -\frac{2\pi}{\gamma} \int_{(5+t)}^{4.75} K_x(0,0,z)\, dz \quad . \tag{44}$$

The new characteristic position offset becomes

$$\Delta x = \frac{2\pi}{\gamma} \int_{-(5+t)}^{5} dz' \int_{-(5+t)}^{z'} K_y(0,0,z)\, dz \qquad \text{and}$$

$$\Delta y = -\frac{2\pi}{\gamma} \int_{-(5+t)}^{4.75} dz' \int_{-(5+t)}^{z'} K_x(0,0,z)\, dz \qquad , \qquad (45)$$

where $K = 1.0$ and $\gamma = 30.35$. The units used for the tables will be radians for angles and non-dimensional lengths for offsets.

The most notable feature in Table 1 is that more tapering does _not_ achieve the best entrance conditions [8,9]. We can see that no tapering achieves the minimum characteristic values. Also, the characteristic angles are fairly insensitive to tapering. This is especially true for the y values. Recall that tapering did little to assuage the asymmetry at the undulator entrance. Although not easy to discern, it appears that if tapering is applied, the best method is a linear taper. This is another surprise as a smooth current taper should produce the smoothest magnetic field transition. Therefore, the optimum winding configuration for wire/wire termination is with no tapering. At the bottom of Table 1 are the absolute values of the ideal injection angle and position offset at z = -5 for the perfect trajectories shown in (38) and (39). The absolute values are used because the simulation and ideal polarizations are not matched.

Characteristic values for various tapering schemes with wire/wire termination.

Table 1 .				
Tapering scheme	θ_x	θ_y	Δx	Δy
No Taper	0.062	-0.003	-0.109	-0.188
1 period taper (linear)	0.063	-0.003	-0.122	-0.207
2 period taper (linear)	0.063	-0.003	-0.135	-0.225
3 period taper (linear)	0.063	-0.003	-0.146	-0.244
3 period taper (tangent function)	0.063	-0.003	-0.153	-0.243
3 period taper (smooth curve)	0.063	-0.003	-0.150	-0.243
4 period taper (linear)	0.064	-0.003	-0.156	-0.262
4 period taper (tangent function)	0.064	-0.003	-0.171	-0.261
4 period taper (smooth curve)	0.064	-0.003	-0.166	-0.261
5 period taper (linear)	0.064	-0.003	-0.165	-0.280
5 period taper (tangent function)	0.064	-0.003	-0.1?4	-0.279
5 period taper (smooth curve)	0.064	-0.003	-0.178	-0.280
I Ideal values I	0.033	0	0	0.170

Next try the characteristic test on loop/wire termination to find if our original assumptions are true as shown in Table 2.

Characteristic values for various tapering schemes with loop/wire termination.

Table 2 .				
Tapering scheme	θ_x	θ_y	Δx	Δy
No Taper	0.056	-0.003	0.108	-0.184
1 period taper (linear)	0.057	-0.003	0.117	-0.203
2 period taper (linear)	0.059	-0.003	0.124	-0.221
3 period taper (linear)	0.059	-0.003	0.132	-0.239
3 period taper (tangent function)	0.059	-0.003	0.132	-0.239
3 period taper (smooth curve)	0.059	-0.003	0.132	-0.239
4 period taper (linear)	0.060	-0.003	0.139	-0.258
4 period taper (tangent function)	0.060	-0.003	0.140	-0.257
4 period taper (smooth curve)	0.060	-0.003	0.140	-0.257
5 period taper (linear)	0.061	-0.003	0.146	-0.276
5 period taper (tangent function)	0.061	-0.003	0.147	-0.276
5 period taper (smooth curve)	0.061	-0.003	0.147	-0.276
I Ideal values I	0.033	0	0	0.170

The most notable feature in Table 2 is that despite the enhanced symmetry in the fields noted with loop termination, no tapering is still indicated as optimum. Because of the increased symmetry, all values can be seen to be less than their wire/wire counterparts. The characteristic position offset in the x direction has reversed sign. As in wire/wire termination, if tapering is applied, the linear taper is slightly better. It is surprising to note that despite the increased symmetry, the values obtained are not significantly different from the wire/wire values. This implies that the electron trajectories will show an improvement in imposed input conditions, but not to any drastic extent. We will see if this is true when the simulation is carried out. Again, at the bottom of Table 2, the ideal injection angle and position offset are provided for reference.

The last characteristics determined are for loop/loop termination as shown in Table 3. Table 3 shows a repeat of all the trends seen for loop/wire termination. As anticipated, the increased symmetry has resulted in smaller characteristic values for all methods explored. The inference here is that loop/loop termination will provide the smallest position and angle offsets required for optimum electron injection. The characteristic values found are close to the ideal values shown at the bottom of the Table. All terminations indicate that the optimum tapering scheme is no taper at all. We now need to apply this knowledge to an electron trajectory simulation.

Characteristic values for various tapering schemes with loop/loop termination.

Table 3 .				
Tapering scheme	θ_x	θ_y	Δx	Δy
No Taper	0.037	-0.003	0.042	-0.180
1 period taper (linear)	0.037	-0.003	0.041	-0.198
2 period taper (linear)	0.037	-0.003	0.040	-0.216
3 period taper (linear)	0.037	-0.003	0.038	-0.234
3 period taper (tangent function)	0.037	-0.003	0.038	-0.234
3 period taper (smooth curve)	0.037	-0.003	0.038	-0.234
4 period taper (linear)	0.037	-0.003	0.036	-0.252
4 period taper (tangent function)	0.037	-0.003	0.037	-0.252
4 period taper (smooth curve)	0.037	-0.003	0.037	-0.252
5 period taper (linear)	0.037	-0.003	0.034	-0.270
5 period taper (tangent function)	0.037	-0.003	0.035	-0.269
5 period taper (smooth curve)	0.037	-0.003	0.035	-0.270
I Ideal values I	0.033	0	0	0.170

69

Now that the optimum tapering scheme for each termination has been determined, we simulate the electron beam trajectories. The electrons are started at the characteristic deflection angle and position offset indicated for the optimum tapering configuration. Several simulations are run to minimize the input conditions necessary to achieve helical motion centered down the z axis. The first example is wire/wire termination shown in Figure 45.

Figure 45 shows the superposition of the electron beam trajectories on the same design as in Figure 42 which has wire termination used at the entrance and exit of the undulator. The beam must enter in the correct position and angle in order to get the beam to stay in the undulator. After some optimization, the input position and angle parameters, starting back at $z_o = -5$ away from the undulator entrance, are found to be $x_o = 0.45g$, $y_o = -0.8g$, $\theta_x = 0$ and $\theta_y = 0.035$ where g = 2mm. When additional tapering is used, the input parameters become even more extreme. If no offsets are used, the asymmetry in the entrance fields sends the beam into the side of the undulator at $N = 4$ periods. The stray fields resulting from wire termination at both ends are not suitable for practical FEL application. Loop termination provides a more symmetrical field composition, and should give a smaller deflection to the incoming electron beam.
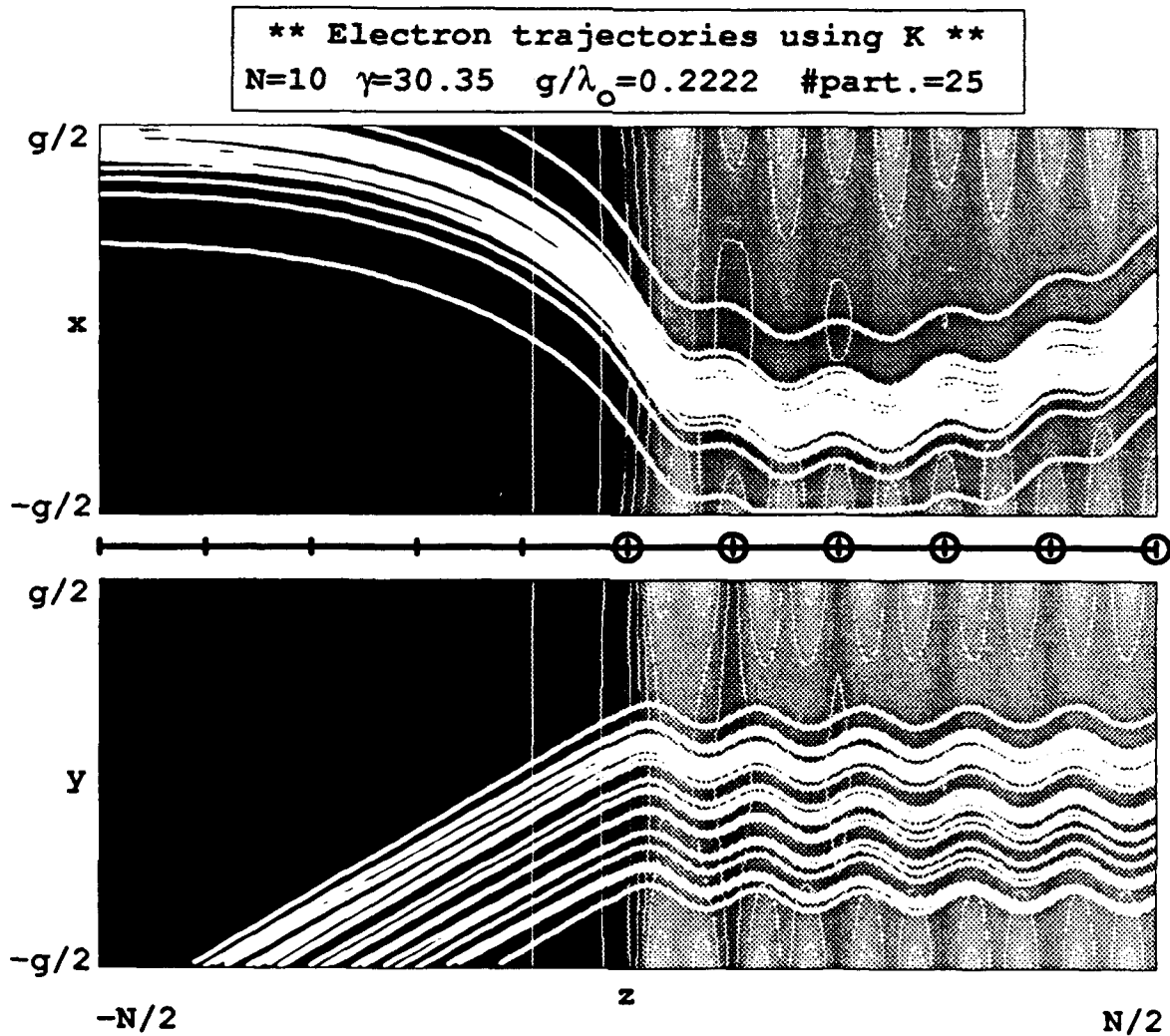
Figure 45 .

Electron trajectories overlaid on K field background

for wire/wire termination, no taper.

If loop termination is used at the entrance of the undulator and wire termination is used at the exit, the result is Figure 46. The input angle parameters for this design, starting at $z_o = -5$, become $\theta_x = -0.027$ and $\theta_y = 0.035$. The loop termination reduces the large magnitude field reversal in the x plane experienced by the electrons traversing the undulator entrance and thus, the resultant trajectories are much more like those shown in the y plane (electron beam deflected by a single angle at the entrance to undulator). Thus, only the angle offsets are given. The electron beam entrance requirements are reduced, especially in the x plane as predicted by Fajans [8]. Unfortunately, the y plane still suffers from about the same extreme position and angle offsets. It is possible that, because of the compact FEL dimensions, the exit leads are imposing an unexpectedly significant effect on the entrance stray fields. If loop termination could be applied to the exit leads, and the wires taken from the undulator in a coaxial cable, the effect of the wire exit termination would be reduced, and may ameliorate the entrance parameters.
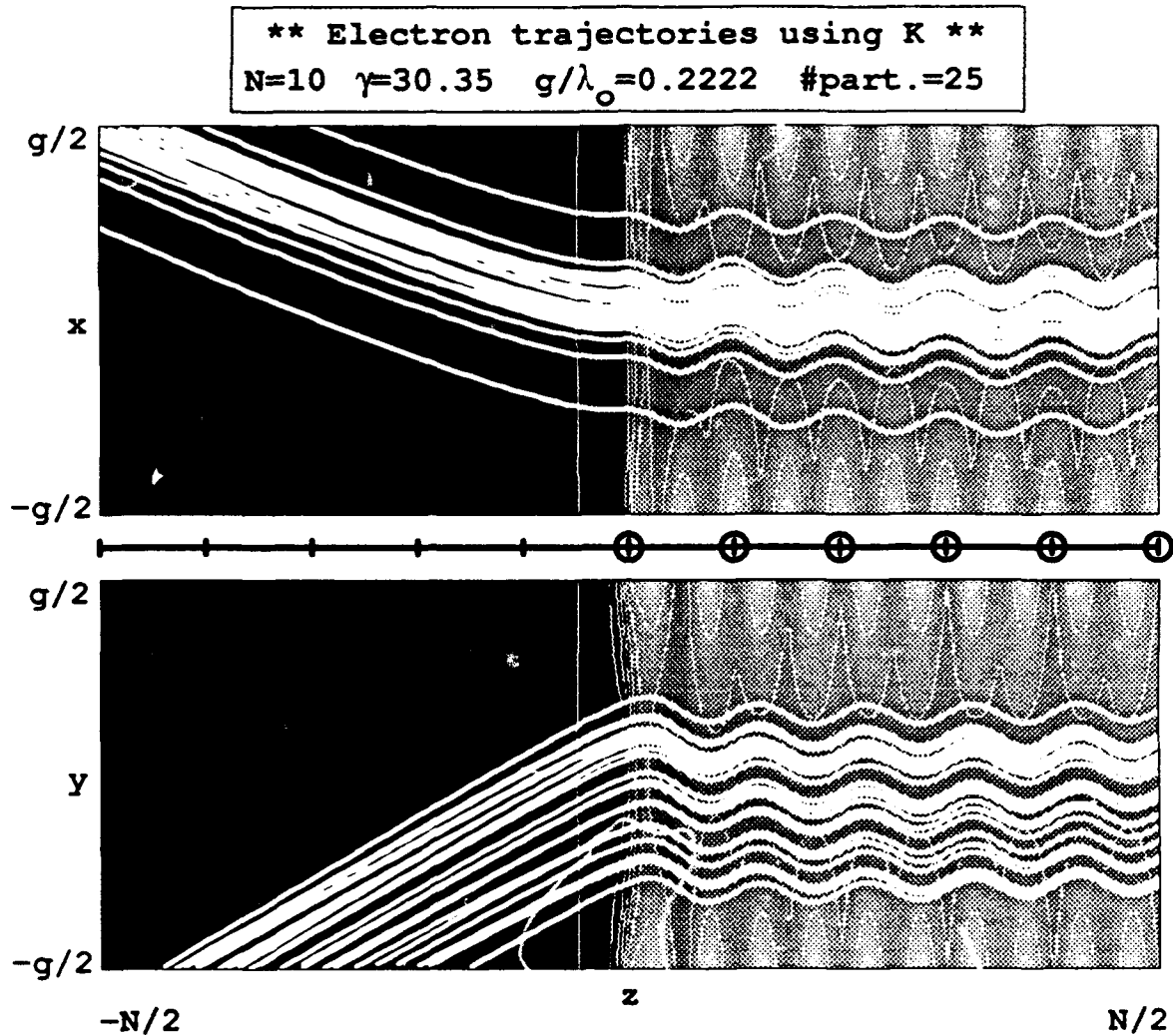
** Electron trajectories using K **
N=10 γ=30.35 g/λ_o=0.2222 #part.=25

Figure 46 .

Electron trajectories overlaid on K field background

for loop/wire termination, no taper.

Loop termination is applied to the undulator entrance and exit leads
shown in Figure 47. It is found that the minimum angle and position offsets are
achieved when no tapering is used. The input parameter angles, starting from
$z_o = -5$, become $\theta_x = -0.012$ and $\theta_y = 0.035$. The result is that the input

73

electron beam parameters are nearly at the ideal injection angle of $\theta_x = 0.033$ calculated previously. This is obviously the best winding design.
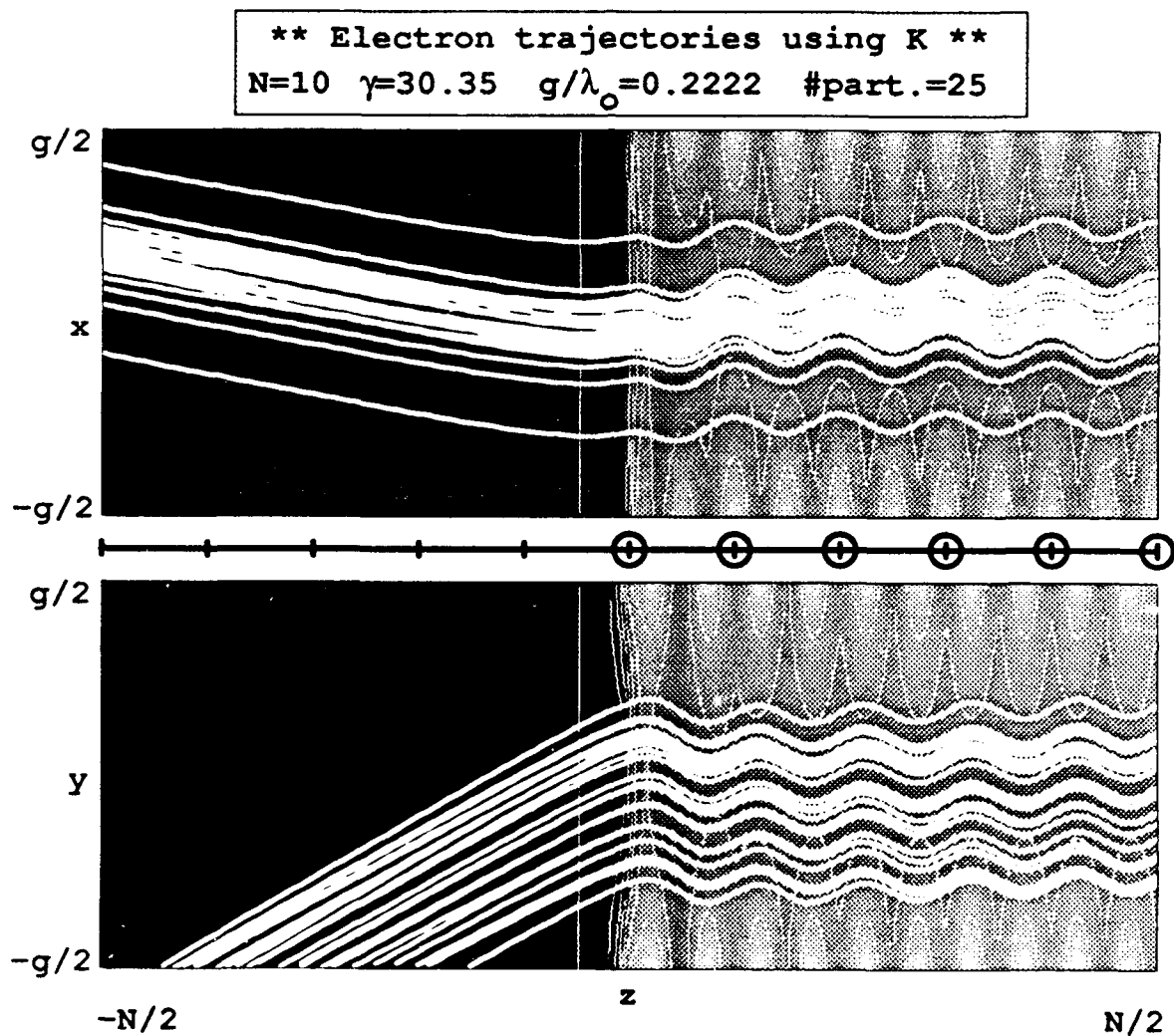

Figure 47 .

Electron trajectories overlaid on K field background

for loop/loop termination, no taper.

IV. CONCLUSION OF OPTIMUM DESIGN

The aim of this paper was to do a computer simulation of the fields and electron trajectories associated with an FEL. The compact FEL design used was originally proposed as a method of achieving shorter wavelength light output from an FEL. The simplicity of design lent itself to easy modeling and because of the small dimensions, was assumed to accentuate the stray fields at the end of the undulator. These stray fields have not been extensively investigated as they are a small effect in more common FELs. This turned out to not be the case with the compact FEL. This determination was reached with many different types of representations of the magnetic fields associated with the device. The minimum angle and position offset imposed on the electron beam for smooth entry down the center of the undulator was used as the determining factor in the selection of the optimum design modification.

All the design modifications considered show that stray fields at the ends of bifilar helical undulators with realistic wire leads cause serious deflections of the entering electron beam. Even with a termination that achieves improved symmetry in the magnetic field structure, loop termination, the discontinuity in the fields imposed by the termination itself with any kind of current tapering results in significant perturbations to the electron trajectories. The optimum design of those presented is the loop termination design at the undulator entrance and exit with no taper. This design achieves the smallest position and angle offset requirements on the input electron beam, and would be the least complicated to construct.

LIST OF REFERENCES

[1] Pines, David, editor, et. al., *Reviews of Modern Physics*, Vol. 59(3), Part II, July 1987, p s33-s35.

[2] Siegman, Anthony, **Lasers**, University Science books, 1986, p 2.

[3] Colson, William, *Free Electron Laser Theory*, PhD thesis at Stanford University, 1977.

[4] Hecht, Eugene, **Optics**, Addison-Wesley Publishing Co., 1987, p 272.

[5] Colson, W. B., Pellegrini, C. and Renieri, A., editors, **Free Electron Laser Handbook**, Chapter 3, p 6,7.

[6] Blewett, John P. and Chasman, R., *Orbits and Fields in the Helical Wiggler*, Journal of Applied Physics, Vol. 48(7), July 1977, p 2698.

[7] Warren, Roger W. (LANL), private communication September 1989.

[8] Fajans, J., *Journal of Applied Physics*, Vol. 55(1), January 1984, p 43-50.

[9] Elias, L. R. and Madey, J. M., *Superconducting helically wound magnet for the free-electron laser*, Rev. Sci. Instrum., Vol. 50(11), November 1979, p 1335-1340.

[10] Gould, H. and Tobehnik, J., **An Introduction to Computer Simulation Methods Applications to Physical Systems Part 1**, Addison-Wesley Publishing Co., 1988, p 38.

INITIAL DISTRIBUTION LIST

1. Defense Technical Information Center   2
   Cameron Station
   Alexandria, Virginia 22304-6145

2. Library, Code 52   2
   Naval Postgraduate School
   Monterey, California 93943-5002

3. Professor William B. Colson, Code PH/Cw   9
   Department of Physics
   Naval Postgraduate School
   Monterey, California 93943-5000

4. Professor Fred Ramon Buskirk, Code PH/Bs   1
   Department of Physics
   Naval Postgraduate School
   Monterey, California 93943-5000

5. Professor K. E. Woehler Code PH/Wh   1
   Chairman, Department of Physics
   Naval Postgraduate School
   Monterey, California 93943-5000